IMPACT PROPERTIES OF AISI 316L STAINLESS STEEL REPAIRED BY DIRECTED ENERGY DEPOSITION (DED) ADDITIVE MANUFACTURING PROCESS

By

SOUMYA MANDAL

Bachelor of Engineering in Mechanical Engineering

Rajshahi University of Engineering & Technology

Rajshahi, Bangladesh.

2013

Submitted to the Faculty of the
Graduate College of the
Oklahoma State University
in partial fulfillment of
the requirements for
the Degree of
MASTER OF SCIENCE
December, 2019

IMPACT PROPERTIES OF AISI 316L STAINLESS STEEL REPAIRED BY DIRECTED ENERGY DEPOSITION (DED) ADDITIVE MANUFACTURING PROCESS

Thesis Approved:

Dr. Sandip P. Harimkar

Thesis Adviser

Dr. Shuodao Wang

Dr. Ranji Vaidyanathan

ACKNOWLEDGMENTS

First and foremost, praises and thanks to God, the Almighty, for his showers of blessings throughout my research work to complete the research successfully.

I want to express my deep and sincere gratitude to my advisor Dr. Sandip P. Harimkar, for allowing me to join his research group and guiding me to do good research. It was a great privilege and honor to work under his guidance. Without his immense support, trust, and guidance, it would not have been possible to complete the research successfully. I am grateful to him. I want to extend my heartfelt thanks to him and his family.

I earnestly convey my thanks to Dr. Shuodao Wang and Dr. Ranji Vaidyanathan for accepting to be my thesis committee members instantly with all kindness when I approached them.

I also thank the Vice President research (VPR), Oklahoma State University, for supplying the developments of the additive manufacturing facility used in this work.

I would like to thank my parents, whose love and guidance are with me in whatever I pursue. They are the ultimate role models. I wish to thank my loving little sister, who provides me unending inspiration. I would like to acknowledge my colleagues and friends for their help and support.

Name: SOUMYA MANDAL

Date of Degree: DECEMBER, 2019

Title of Study: IMPACT PROPERTIES OF AISI 316L STAINLESS STEEL REPAIRED BY DIRECTED ENERGY DEPOSITION (DED) ADDITIVE MANUFACTURING PROCESS

Major Field: MECHANICAL AND AEROSPACE ENGINEERING

Abstract: Directed Energy Deposition (DED) is considered as one of the potential processes for metallic structural repairs. In this work, the impact properties of the repaired stainless steel 316L were investigated. The repair was performed by depositing commercially available stainless steel 316L metal powder on the stainless steel 316L substrate using the DED process (LENS$^{@}$ process). Strong bonding between the deposited layers and substrate and also between the layers in the deposited zone was observed under the proper selection and optimization of processing parameters. Results showed that the microstructure of the repaired zone generally consists of columnar and equiaxed grain structure. Heat Affected Zone (HAZ) provided the highest microhardness about 218HV, whereas the microhardness of the repaired zone and substrate was within the ranges of 192-209HV and 168-198HV, respectively. The impact properties of the repaired specimens were compared with the wrought stainless steel 316L (as-received). The average impact energy absorbed by the as-received specimens was higher than the repaired specimens. Moreover, the impact energy absorbed by the AM (subsize) and repaired (subsize) specimen were compared with the as-received specimens. The fractured surface morphology of both repaired and as-received specimens was also studied.

TABLE OF CONTENTS

LIST OF TABLES

LIST OF FIGURES

CHAPTER 1

INTRODUCTION

1.1 Importance of Metallic Structures Repair

Metallic structures experiences load, thermal stresses, corrosion, and other direct and indirect impacts throughout their lifetime. These are the major reasons for the failure of the metallic structures [1, 2]. Defects in the metallic structures can negatively affect the in-service operation performance and thus result in economic loss and safety risk [3, 4]. In this type of situation, a repair can play an important role. Although it is not possible to achieve similar results as a new metallic structure, it is beneficial from the economic and environmental point of view [5]. It requires a lot of energy to manufacture a material product from starting raw materials, resulting in the emission of greenhouse gas (GHG), which is one of the main causes of global warming. About 30% of the GHG comes from material processing [6]. A possible way to mitigate the rate of GHG emissions is to reduce the rate of material processing, and it can be achieved by introducing effective repair processes. Moreover, the selection of effective repair processes will save money and operation time [7].

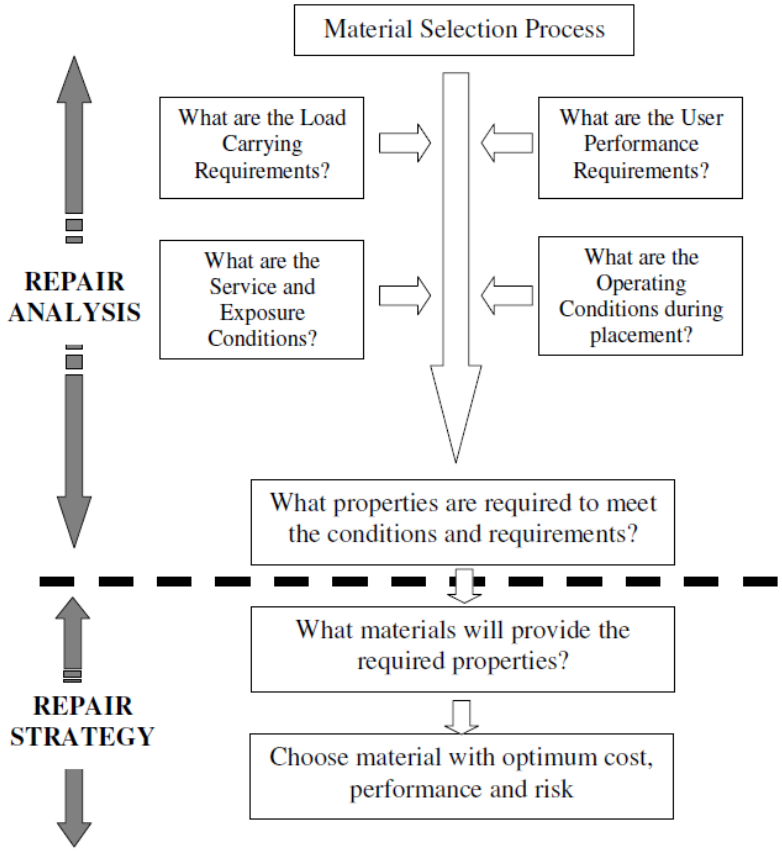

Figure 1: Flowchart showing the procedure of selecting repair materials [8].

It is difficult to maintain the original quality of the metallic structure through repair, but the development of effective repair processes is likely to reduce the quality difference between the new and repaired metallic structures. The selection of materials plays an important role in repairing metallic structures and achieving acceptable performance. **Figure 1** represents a flowchart showing the process of selecting materials for repairing metallic structures. Materials for repairing metallic structures should be selected based on substrate properties and the working area conditions. Therefore, it is a challenging task to select proper materials for repairing. Moreover, it is advisable to select the same repair materials as the substrate to achieve the preferred performance from the repaired metallic structure.

1.2 Material Selection

1.2.1 Engineering Steels

Steels are mainly composed of iron and carbon. The percentage of carbon varies from 0.06%-2.0% in steels. The carbon percentage variation is done to control the physical and chemical properties of the steels. Various grades of steels are produced to satisfy the necessity of different applications. Four broadly categorized steels are described in **Table 1** for better understanding.

a) Carbon Steels: The main element of carbon steels is carbon. Moreover, carbon steels contain a traceable amount of other elements (1.65% manganese, 0.6% silicon, and 0.6% copper). Based on the carbon content, carbon steels can be classified into low carbon steels (up to 0.3% carbon), medium carbon steels (0.3%-0.6% carbon), and high carbon steels (0.6% carbon).

b) Alloy Steels: These contain various alloying elements such as manganese, silicon, nickel, titanium, copper, chromium, aluminum. By varying the percentage of these alloying elements, it is possible to control the properties of alloy steels (e.g., hardenability, corrosion resistance, strength, or ductility).

c) Tool Steels: Tool steels consist of tungsten, molybdenum, cobalt, and vanadium. Some of the widely used tool steels are hot work tool steels, cold work tool steels, shock resistant tool steels, and high-speed tool steels.

d) Stainless Steels: The main alloying elements of stainless steels is chromium (10%-20%). Depending on the crystalline structure, stainless steels can be divided into austenitic, ferritic, and martensitic steels. Austenitic steels contain 18% chromium, whereas ferritic contains 12%-17%, and Martensitic contains 11%-17% chromium, respectively. The non-magnetic and non-heat treatable property makes austenitic steels superior to the other two types of stainless steels.

Table 1: The properties of stainless steels at room temperature [9].

Properties	**Carbon Steels**	**Alloy Steels**	**Stainless Steels**	**Tool steels**
Density (1000 kg/m^3)	7.85	7.85	7.75-8.1	7.72-8
Elastic Modulus (GPa)	190-210	190-210	190-210	190-210
Poisson's Ratio	0.27-0.3	0.27-0.3	0.27-0.3	0.27-0.3
Thermal Expansion (10^{-6}/K)	11-16.6	9-15	9-20.7	9.4-15.1
Thermal Conductivity (W/m-K)	24.3-65.2	26-48.6	11.2-36.7	19.9-48.3
Specific Heat (J/kg-K)	450-2081	452-1499	420-500	------
Electrical resistivity (10^{-9}W-m)	130-1250	210-1252	75.7-1020	------
Tensile strength (MPa)	276-1882	758-1882	525-827	640-2000
Yield Strength (Mpa)	186-758	366-1793	207-552	380-440
Elongation (%)	10-32	4-32	12-40	5-25
Hardness (Brinell 3000kg)	86-388	149-627	137-595	210-620

1.2.2 General Properties of stainless steels

Each grade and category of stainless steels is easily distinguishable by its unique advantages and properties. Besides, they are well suited and widely demanded for modern day challenges. **Figure 2** represents the properties of stainless steels, which are briefly discussed below.

Figure 2: Characteristic properties of stainless steels.

a) Aesthetic: Stainless steels are called aesthetic materials because of their good surface finish quality. Architects often use stainless steels for interior design and urban furniture production.

b) Mechanical property: Stainless steels are very popular for construction and building applications because of their attractive mechanical properties namely good ductility/toughness, and hardness/strength property.

c) Resistance to Fire: Stainless steels exhibit a critical temperature of 800 °C and do not emit any toxic fumes during burning which makes stainless steel suitable for most of the construction applications.

d) Corrosion Resistance: A passive layer of chromium oxide is formed on the surface of the stainless steels through the combination of chromium and oxygen. This passive layer on the stainless steels acts as a protective layer from corrosion.

e) Cleanability: The surface of the stainless steels can be cleaned easily by using normal detergents or soap powders without any damage.
f) Recycling: Stainless steels are called “green materials” because the recycling rate of stainless steels is almost 100%.

Some of the other properties of stainless steels are resistance to creep and oxidation, and strength at low temperatures.

1.2.3 AISI 316L Stainless Steel

The impressive performance at high temperature, high corrosion application, and good manufacturability makes AISI 316L stainless steel superior over other stainless steels. Moreover, the cost of stainless steel 316L is reasonably low. These properties establish the stainless steel AISI 316L as one of the most popular and extensively demanded materials for manufacturing different metallic structures [10]. The position of the AISI 316L stainless steel on the Schaeffer diagram based on composition is illustrated in **Figure 3** [11, 12]. The composition of stainless steel 316L is represented in **Table 2** [13]. The AISI 316L stainless steel is selected as both substrate/plate and the depositing powder materials to perform the repair in this work.

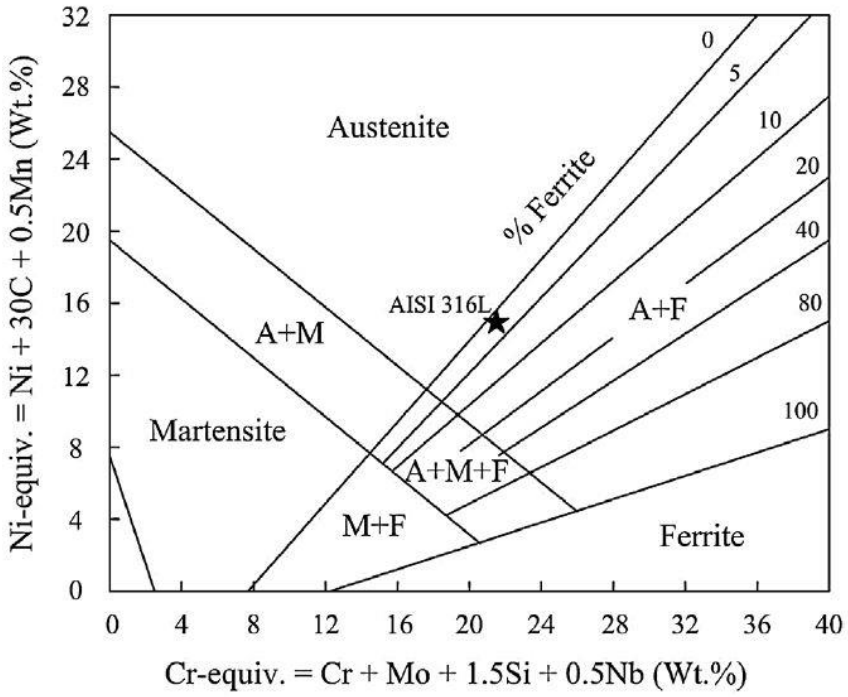

Figure 3: Schaeffer diagram showing the composition of the AISI 316L stainless steel [11, 12].

Table 2: Composition of stainless steel 316L (weight percentage) [13].

Elements	Percentage Composition (wt%)
Carbon	0.03
Chromium	16-18
Copper	0.50
Iron	Balance
Manganese	2.00
Molybdenum	2-3
Nitrogen	0.10
Nickel	10-14
Oxygen	0.10
Phosphorus	0.045
Sulfur	0.03
Silicon	0.75

1.3 Different Repair Processes

The requirement of the precise and efficient approach to repair, along with the low investment, has initiated the developments of the repair processes over the years. In all repair processes, the bonding between the deposited materials and the substrate, and also in between the deposited layers, is the main concern. Metallurgical bonding generally depends on the deposition time, patterns, and volume. In some processes, post repair processing also plays a very significant role. Once the damaged area of the metallic structure is identified, it is always advisable to detect the initial flaws through continuous observations and inspections. Before performing the repair, the damaged area of the metallic structure should be cleaned up properly to remove rust, oils, and pigments from the surface. The selection of cleaning processes is dependent on the repair processes and accessibility towards the damaged area, which has to be repaired. **Figure 4** represents the different processes that are widely utilized in repairing metallic structures. Among different processes, cold spray (CS) [14], arc welding [15], and vapor deposition [16] are considered as the conventional repair processes, whereas the Directed Energy Deposition (DED) and Powder Bed Fusion (PBF) are considered as the AM based repair processes.

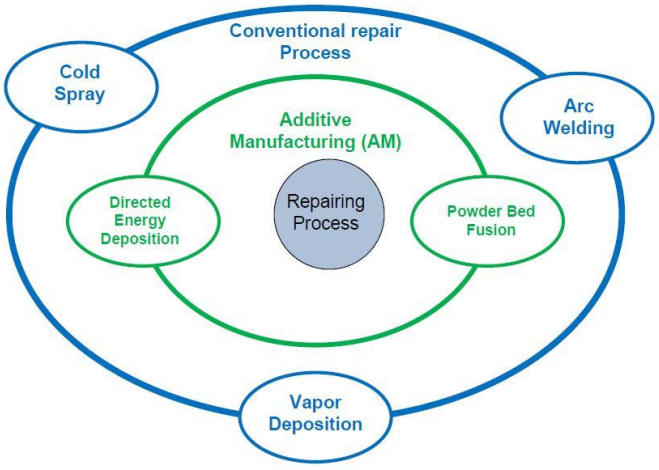

Figure 4: Different processes for structural repairs.

Cold spray (CS) has received a lot of interest as a conventional repair process over the last couple of years, and many research works have been carried out in this area [17-21]. In the CS process, powder particles are sprayed at a high velocity on the substrate, and the powder particles are bonded with the substrate due to localized deformations. **Figure 5** shows a schematic diagram of the cold spray operation. The deposition depends on the kinetic energy of powder particles, whereas the bonding in between the deposited powder and the substrate depends on the localized plastic deformation. To repair the damaged area of the metallic structures successfully, the feedstock powder particle must have to be sprayed at a critical impact velocity [22]. **Table 3** represents the comparison between the CS, DED, and PBF as a repair process.

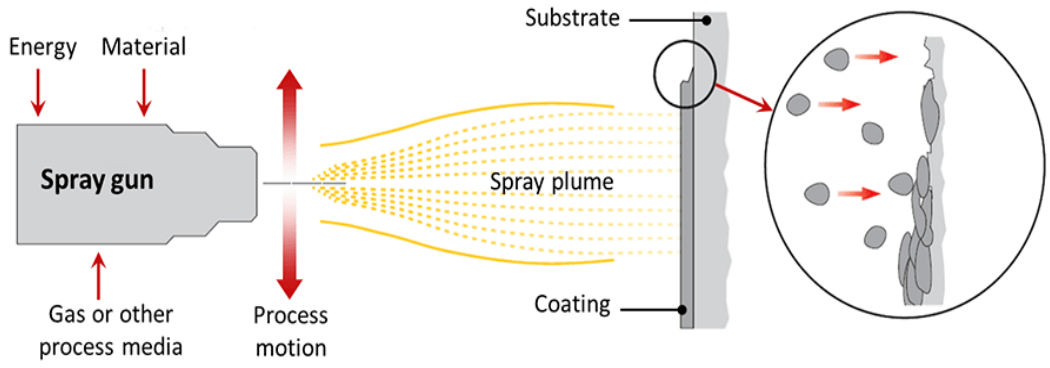

Figure 5: Schematic diagram of the cold spray process [17].

Strong bonding between the substrate and the deposited area is the prominent requirement for getting better performance from the repaired metallic structures. Conventional repair processes, like arc welding and vapor deposition, provide poor bonding in between the substrate and deposited area. Besides, the cold spray provides better bonding between the substrate and deposited zone, but it is not suitable for repairing high strength materials. In cold spray, bonding between the substrate and deposited area depends on the localized plastic deformation of the deposited powder particle. So, it is challenging to obtain a dense deposition on the damaged area

of the metallic structures made of high strength materials [17]. Moreover, the velocity of the deposited powder particle should be controlled for obtaining strong bonding between the substrate and deposited area. The bonding between the substrate and deposited area can be improved with the introduction of post heat treatment. On the other hand, the DED process does not have any issue in repairing the high strength materials. Besides, DED provides better mechanical properties without the post-heat treatment in comparison to cold spray.

Table 3: Comparison between the CS, PBF, and DED repair processes [22].

Process Characteristic	**Repair Process**		
	CS	**PBF**	**DED**
Powder Feed Mode	Directed Deposition	Powder Bed	Directed Deposition
Feedstock Limitation	Difficulty processing high hardness and strength materials	Difficulty processing high hardness and strength materials	Difficulty processing high hardness and strength materials
Powder melting	No	yes	Yes
Product Size	Large	Limited	Large
Dimension Accuracy	Low	High	High
Mechanical properties	Low	High	High
Production Time	Short	Long	Long
Suitable for Repairing	Yes	No	Yes

1.4 Directed Energy Deposition (DED) as a Repair Process

Additive Manufacturing (AM) has made significant progress over the years in terms of design freedom, fabricating complicated and accurate geometry, reducing metal wastage, and rapid prototyping. According to the American Society for Testing and Materials (ASTM), "AM is a process of joining materials to make an object from 3D model data, usually layer upon layers, as opposed to subtractive manufacturing methodologies" [23-25]. AM processes have received a lot of interest and success as a repair process over the last couple of years. The AM based DED process outperformed the PBF process in repairing metallic structures [6, 26].

Directed Energy Deposition (DED) is the superior repair process over other processes because of the controlled and confined heat input, controlled rate of deposition, flexibility in building, accurate and higher deposition rate establish [27]. Moreover, the DED process is utilized for repairing functionally graded parts [28, 29]. In DED, metal powder is supplied from the feeders with the carrier gas towards the damaged area of the metallic structures. When the metal powder comes into contact with the laser beam, the metal powder melts and deposits on the damaged area. A lens is used to control the focusing of the laser power, whereas the nozzle is used to control the powder flow rate. The damaged area is allowed to move under the laser power and power feed system, which is controlled by the computer unit [30, 31]. **Figure 6** shows the schematic diagram of the DED process, along with the standard molten pool characteristics [32, 33].

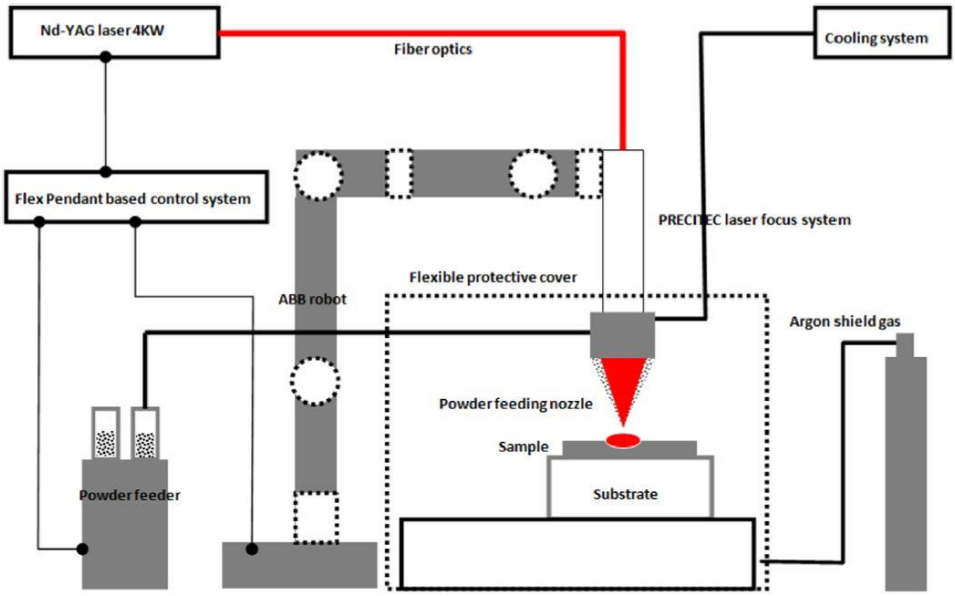

(a)

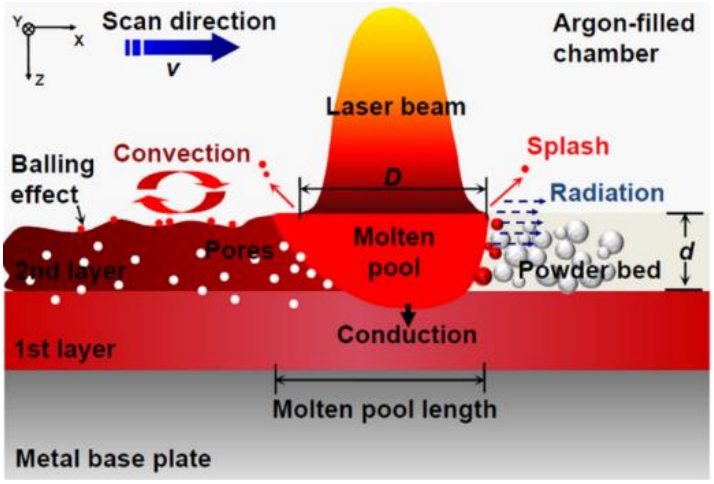

(b)

Figure 6: The schematic diagram of the (a) DED process (LENS®), (b) molten pool [32, 33].

CHAPTER 2

LITERATURE REVIEW

2.1 Previous Work on Repairing using DED Process

Significant research work has been published concentrating on repairing metallic structures utilizing the DED process. *Petrat et al.* [34] successfully demonstrated a gas turbine burner repaired by utilizing the DED process. *Kumar et al.* [35] studied the effects of processing parameters in repairing metallic structure made of Inconel 718, where the commercially available Inconel 718 metal powders were used. In their work, the optimal processing parameters were selected by using Taguchi L9 orthogonal array method for getting better repair results. *Kistler et al.* [36] investigated the effect of processing parameters and processing conditions on repairing. The results showed that every processing parameter independently and collectively influences the microstructure and mechanical properties of the repaired structure. Their work also focused on quantification and identification of defects that were formed during the repair.

The effect of groove size and shape on repairing had been investigated by *Benjamin Graf et al.* [37], where the repairs were performed utilizing the DED process. Better fusion and fewer defects on the repaired grooves had been obtained for the wider grooves. *Paydas et al.* [38] investigated

effects of groove thickness in repairing Ti-6Al-4V substrate by using the DED process. Besides, they discussed the change of microstructure with the change of building strategy during the repair process. The microstructure was homogeneous for low incident energy whereas the microstructure was heterogeneous for high incident energy. The tensile property and the hardness of the repaired components had been analyzed and compared with the substrate. *Pinkerton et al.* [39] studied the microstructure, tensile property, and hardness of the repaired specimens for two different slots or groove geometry (one rectangular and another triangular). In both cases, H13 hot work tool steel substrate was repaired depositing H13 powder using the DED process. Moreover, the defects in between the substrate and deposited area had been investigated. *Song et al.* [40] repaired the trapezoidal groove of 304 stainless steel substrate by depositing stainless steel 316L powder followed by surface alloying with WC powder. The cladded zone microstructure was dominated by columnar dendritic and equiaxed grains, whereas the alloyed surface was exhibiting supersaturated austenite dendrites and homogeneous inter-dendritic networked carbides. Moreover, the repaired specimen with the highest WC percentage provided better hardness property. *Zhang et al.* [41] repaired a hemisphere shaped defects on the AISI H13 tool steel by depositing Co based alloy powder and analyzed the microstructure of the repaired zone. The columnar dendritic structure was visible near the interface, whereas the inter-dendritic eutectics were visible on the other areas. In this study, tensile and hardness tests were performed, and in both cases, the repaired zone provided the better results.

Marya et al. [42] successfully repaired the four ferrous alloys (UNS G41400 low alloy steel, UNS S41000 martensitic stainless steel, UNS S17400 precipitation strengthened martensitic stainless steel and UNS S32750 super duplex stainless steel) depositing UNS N06625 metal powder and briefly discussed the microstructure and mechanical properties of these repaired samples. Results showed that all of the ferrous parts were repaired successfully with the minimum defects. However, poor martensitic hardening was observed only at the HAZ of UNS S32750 steel. *Sun et*

al. [43] analyzed the microstructure along with the microhardness, Charpy impact toughness, and tensile property of repaired HSLA-100 steel by utilizing the DED process. The result showed that the repaired sample provided better tensile property and lower impact property than the substrate. The fracture surface morphology of the repaired sample had also been discussed. *Sun et al.* [44] reported the influence of metal powder composition on the microstructure and mechanical properties of stainless steel 316L repaired by the DED process. The specimen repaired with powder Fe-0.15C-11.8Cr-0.15Mn-0.2Ni-0.031P-0.56Si-0.05S (wt%) and Fe-0.09C-17.05Cr-1.2Mn-11.28Ni-0.019P-0.46Si-0.09S (wt.%). In terms of Charpy impact toughness and tensile property the later powder (Fe-0.09C-17.05Cr-1.2Mn-11.28Ni-0.019P-0.46Si-0.09S (wt.%)) showed better result whereas the specimen repaired by using former powder (Fe-0.15C-11.8Cr-0.15Mn-0.2Ni-0.031P-0.56Si-0.05S (wt.%)) provided better microhardness. Moreover, the fracture surface morphology of the repaired specimens had been analyzed. *Oh et al.* [26] repaired a damaged hot rolled PBF specimen having grooves of different depth utilizing the DED process and analyzed the metallographic characteristics, microhardness, and tensile property. Results showed that the microhardness of the repaired specimen was higher, whereas the tensile strength of the repaired specimen was lower than the original PBF specimen. The tensile strength of the repaired specimens decreased as the repair depth increases. Moreover, some research work had been carried out to investigate the fatigue behaviors and fracture surface morphology of the specimens repaired by the DED process [45-47].

According to the literature review, impact property is considered as the relevant criteria for investigating the quality of the repaired specimen. **Figure 7** represents the repair strategy and geometry of the repaired specimen prepared for the Charpy impact test reported in the literature. The number of interfaces that exposed the repaired zone to the substrate was more than one and thus caused the fracture away from the repaired zone for some repaired specimen during the Charpy impact test. Unlikely, for some repaired specimen, although the crack started to initiate

from the tip of the notch but propagated through the side interfaces rather than propagating through the repaired zone, which resulted in bad impact property as well as the bad fracture surface morphology of the repaired specimen. Reduction in the number of the interface can be a possible solution for getting better impact property. Although the repair was done by utilizing the DED process but based on the available literature to the best of authors' cognition, previously no such work was performed for getting the better impact property of the repaired specimen applying different repair strategies for reducing the interface effect.

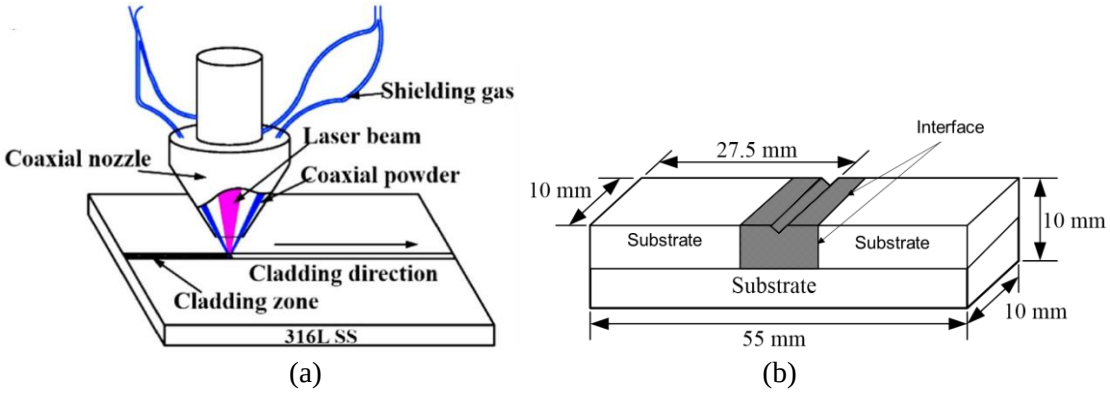

Figure 7: (a) Schematic representation of repairing strategy (b) geometrical representation of repaired specimens for Charpy impact test reported in the literature [43, 44].

2.2 Objectives

The objective of this work is to utilize the DED process for repairing the stainless steel 316L substrate by depositing stainless steel 316L powder and investigate the impact property of the repaired specimen and compare it with the monolithic 316L stainless steel. The repairs are performed by depositing 0.254 mm thick layers on the substrate using optimized laser parameters.

CHAPTER 3

EXPERIMENTAL METHODOLOGY

3.1 Selection of Materials and DED Processing Parameters

Stainless steel 316L powder (commercially known as FE-271-4, Praxair Surface Technologies) having a particle size range of +45μm/-150μm was utilized for performing the repair. Moreover, 6mm thick stainless steel 316L plate (McMaster-Carr) was used as a substrate for this work. All the repairing was carried out by utilizing Optomec (Albuquerque, New Mexico), LENS® 450 XL machine equipped with a 400W IPG Fiber laser system.

The selection and optimization of processing parameters for repairing metallic structures is an important and challenging task that could affect the microstructure evolution of the deposited zone and bonding in between the substrate and deposited area. Seven single lines were deposited on stainless steel 316L substrate as shown in **Figure 8**. The processing parameters, namely laser power, scanning speed, and powder feed rate, were different for each line deposition. **Table 4** represents the selected processing parameters for each line. The selection of the processing parameters for each line was achieved through orthogonal experiments. For lines 1,2,3,4, the scanning speed parameter varied while the other two processing parameters were kept constant, whereas the laser power parameter varied for line 2,5,6,7. Each deposited line showed different height and length based on the fluctuation of processing parameters. Since the height is more sensitive to processing parameters than the width, so the Z direction should be controlled more

precisely than the X and Y direction [48]. **Figure 9 (a)** and **(b)** shows the changes of the height and width with laser power and scanning speed respectively. The height and width of the lines increase with the increasing laser power and decreasing scanning speed [49]. Although at the higher laser power and lower scanning speed, lines provide better results in terms of height and width, it is not always a wise decision to select the highest laser power and lowest scanning speed. There are so many other factors that should be taken into consideration during the selection and optimization of the processing parameters for repairing. The high powder feed rate and lack of sufficient heat input (i.e., low laser power and higher scanning speed) leave powder particles in a partially melted condition inside the molten pool which acts as a source of pore formation. High input of energy is the best possible way to avoid the formation of the pores by

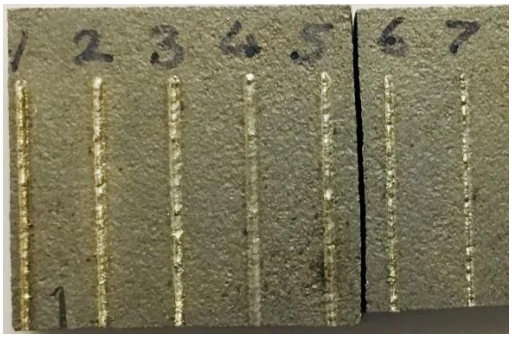

Figure 8: Single line deposition on stainless steel 316L substrate for selecting processing parameters.

Table 4: Processing parameters of seven single lines.

Lines	Scanning Speed (v), (in/min)	Laser Power (P), W	Powder Feed Rate, rpm
1	15	350	6
2	20	350	6
3	25	350	6
4	30	350	6
5	20	300	6
6	20	250	6
7	20	200	6

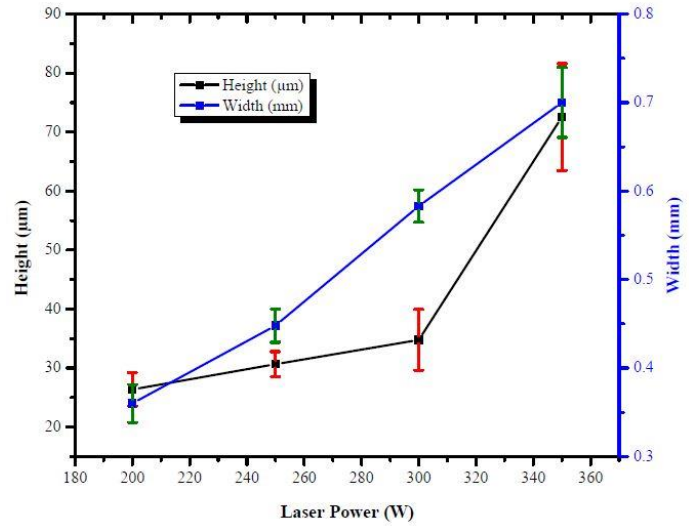

(a)

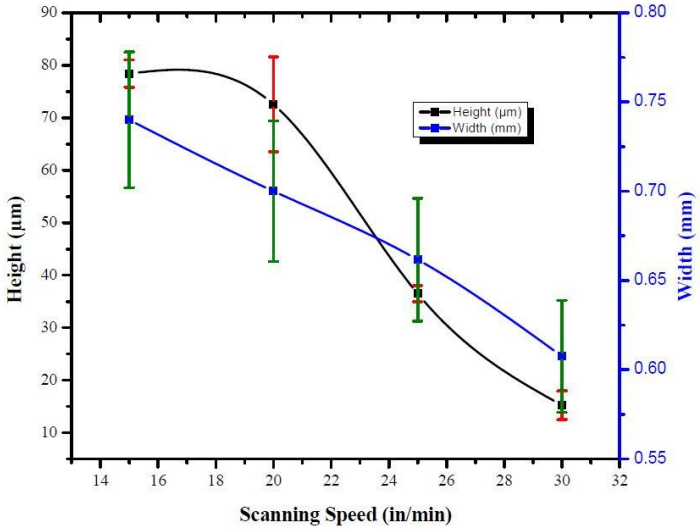

(b)

Figure 9: Variation of height and width of different lines concerning (a) laser power, (b) scanning speed.

melting the powder particle properly. However, thermal stress concentration inside the repaired zone can be caused by the high incident energy which is the possible source of the initiation of microcracks. Since the performance of the repaired specimen is significantly influenced by the processing parameters; the optimization of the processing parameters should be done with proper care. **Table 5** exhibits the optimized processing parameters that were maintained during the repair process. Although all the processing parameters play an important role, in repairing the laser

power and scanning speed are considered as the decisive processing parameters in repairing the AISI 316L stainless steel substrate efficiently and successfully.

Table 5: Optimized processing parameters for repairing the specimen.

Processing parameters		**Values**
Laser Power		350W
Scanning speed		20 in/min
Powder feed rate		6 rpm
Layer Thickness		0.01 inch
Laser Beam		477 micron
Hatch 1	[Distance (mm); Angle (^{0}C)]	0.015; 0
Hatch 2	[Distance (mm); Angle (^{0}C)]	0.015; 90

3.2 Specimens Preparations for Charpy Impact Test

Impact property is considered as one of the important properties in terms of investigating the quality of the repaired specimen. The specimens for the instrumented Charpy impact test were prepared according to the standard ASTM E23-02a. The dimension of the standard repaired specimens and subsize (AM and repaired) specimens were 55mm×10mm×10mm and 55mm×5mm×5mm, respectively. The steps for preparing Charpy impact test specimens are presented below:

1) A stainless steel 316L substrate/plate was taken and the Charpy impact specimens were prepared according to the ASTM standards as shown in **Figure 10(a).**
2) The Optomec (Albuquerque, New Mexico), LENS® 450XL machine, equipped with a 400W IPG Fiber laser system, was utilized for repairing the specimen. Each time before

placing the stainless steel 316L substrate inside the operation chamber, it was polished by using abrasive grit papers followed by sandblasting. Next, the 316L stainless steel substrate was cleaned with the help of acetone to get rid of the possible oxidation and rust. After that, the operation chamber was purged with the help of argon gas to prevent the chance of oxidation [50, 51]. Once the chamber was ready, then the AISI 316L stainless steel powder was deposited on the stainless steel 316L substrate. The repaired specimens were machined from the repaired substrate according to the ASTM standards as shown in **Figure 10(b).** Then a 2mm deep V-notch of root radius 0.25 mm was cut at an angle of 45^0 at the center of the repaired specimen.

3) Similarly, one repaired (subsize) specimen and one fully AM fabricated subsize specimen was machined from the repaired stainless steel 316L substrate according to the ASTM standards for the Charpy impact test. Then a 1mm deep V-notch of root radius 0.25 mm was cut at an angle of 45^0 at the center of the subsize specimens as shown in **Figure 11 (a-c)**. The main difference between the standard and subsize repaired specimen is in the thickness and width while holding the length constant. In the case of the standard repaired specimen, a 5mm deposition was done on the top of the 5 mm substrate, whereas for repaired (subsize) specimen, a 3 mm deposition was done on the top of the 2mm substrate. A computer-aided instrumented Charpy impact tester (Model: Instron 450MPX) was utilized to perform the Charpy impact test on the specimens.

Figures 10 and **11** clearly illustrate that there is only one interface in the prepared repaired specimen that exposes the repaired zone to the substrate. Since there are no side interfaces as reported in the literature, so the possibility of getting fracture away from the repaired zone is lower which is also means the possibility of getting better impact property is higher.

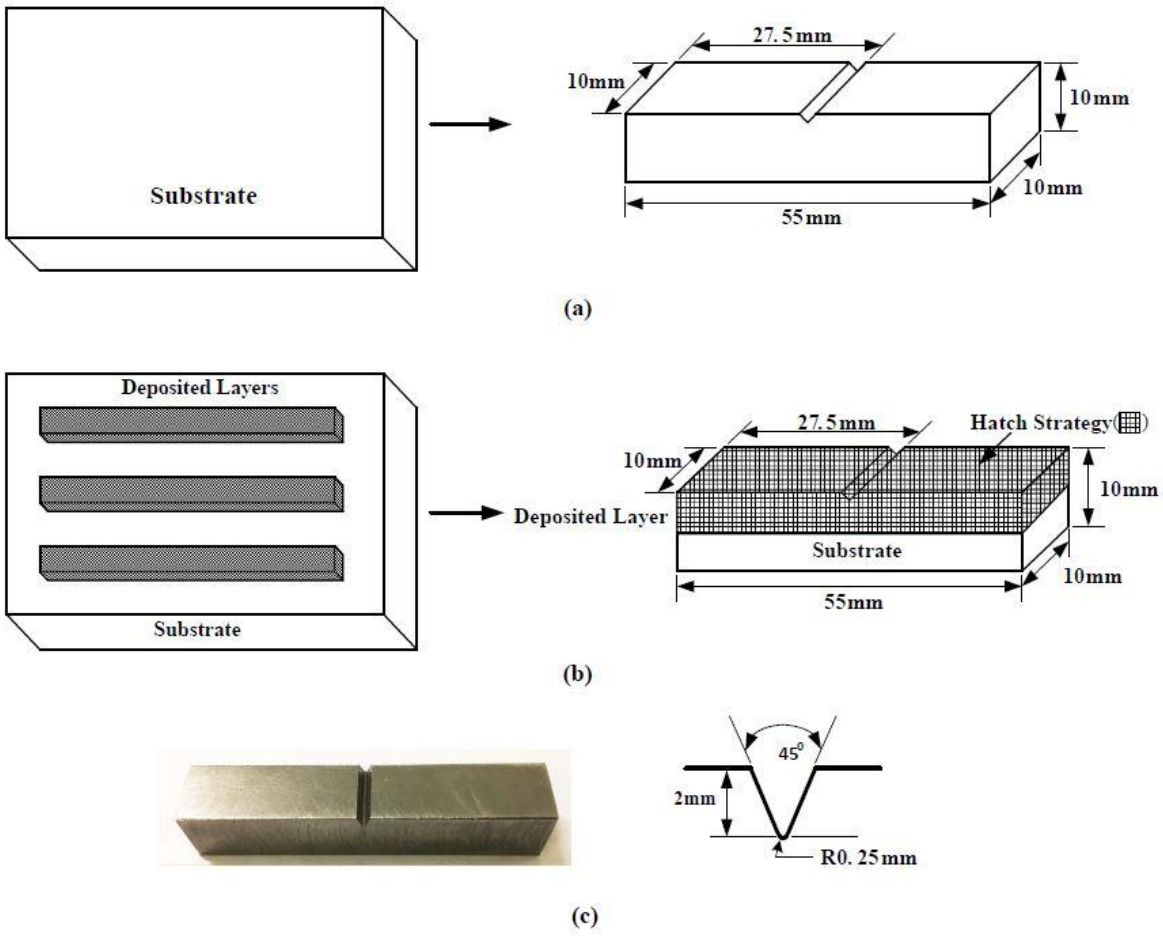

Figure 10: Charpy impact test geometry of (a) as-received specimens, (b) repaired specimens with hatch strategy and (c) the V-notch for standard specimens.

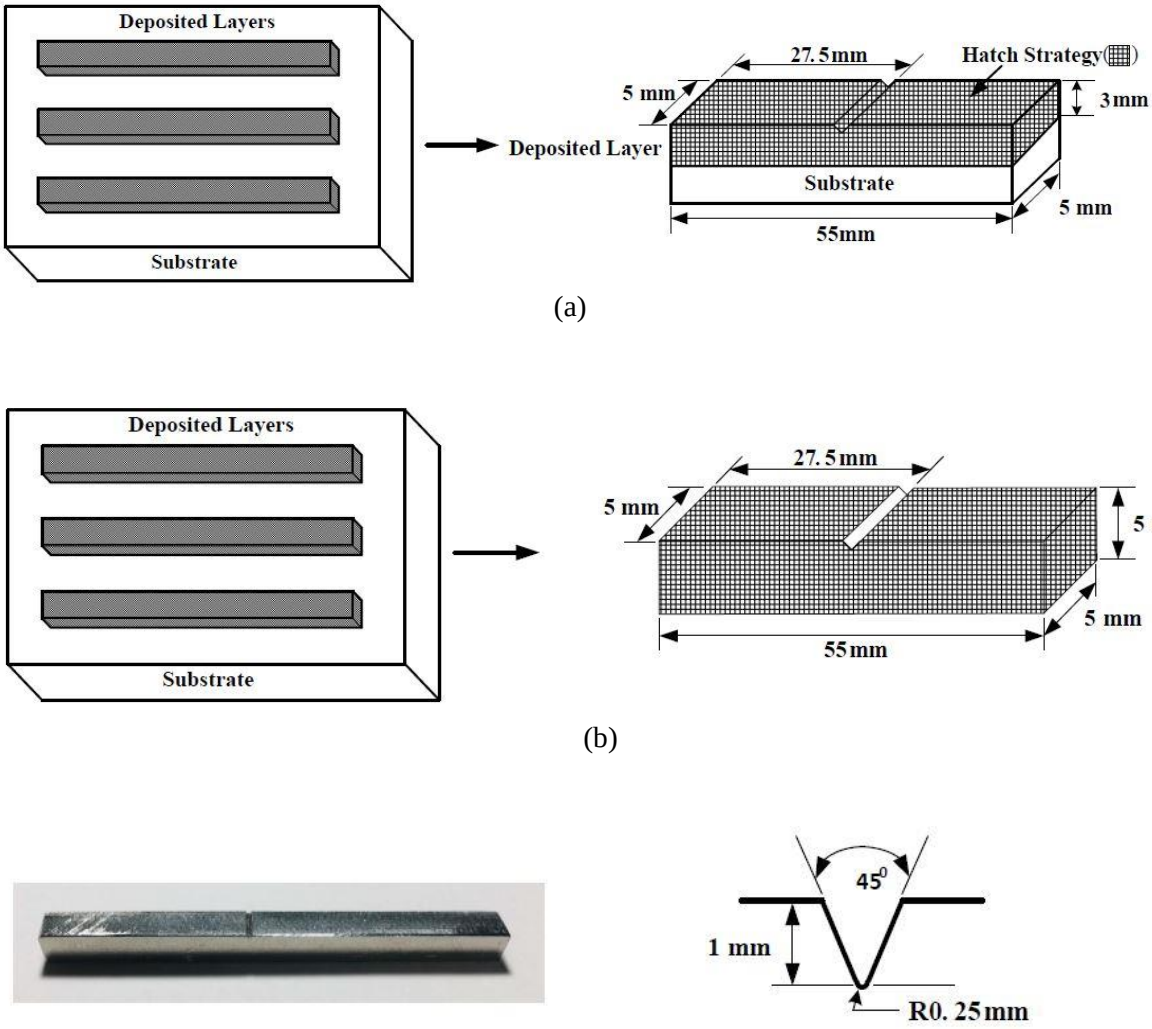

Figure 11: Charpy impact test geometry of (a) repaired (subsize) specimens with hatch strategy, (b) AM (subsize) specimens and (c) the V-notch for subsize specimens [AM=Additive Manufactured].

3.3 Specimens Preparations for Microstructure and Microhardness Analysis

In the followings, the steps for preparing the specimens for microstructure and microhardness analysis are presented:

1) A small cross-sectional area was cut from the standard repaired specimens which was then polished with 240, 600, 800, 1200, 2000 grit size abrasive papers and 0.5-micron alumina paste paper, respectively to get the fine mirror like polished surface. The specimen was etched in a solution of Aqua Regia (30ml distilled water, 20ml HCL, and 15ml HNO_3) for approximately 120 seconds at room temperature. Finally, microstructure analysis was performed using FEI Quanta 600F FE-ESEM (Field Emission Environmental Scanning Electron Microscope). Moreover, the Charpy impact tested specimens were placed under the SEM for studying the fracture morphology of the surface.
2) Similarly, a small cross sectional area was cut from the standard repaired specimen which was then mirror polished by using the same abrasive grit paper following the same steps as it was performed for the SEM specimen preparation. When the specimen was ready, then a Vicker's hardness tester was used for measuring the microhardness.

CHAPTER 4

RESULTS AND DISCUSSIONS

4.1 Effects of Processing Parameters

Having finalized the processing parameters, it is important to analyze the characteristics of the molten pool at different processing parameters. The size and shape of the molten pool changes depending on the variation of the processing parameters. **Figure 12** represents the schematic diagram of the molten pool. Generally, the laser power and the scanning speed are the two main parameters that control the size and shape of the molten pool. At a high laser power and lower scanning speed, a large molten pool is expected which generally circular in shape. Laser power

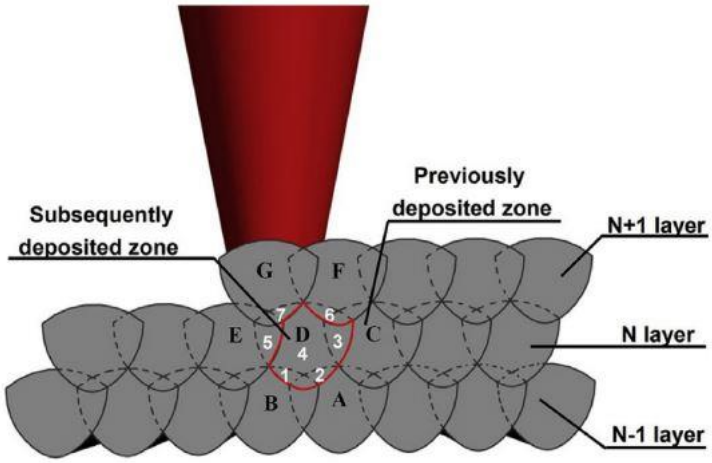

Figure 12: Schematic diagram of molten pool [52, 53].

and the particles usually get more time to interact with each other which would result in more time to solidify. On the other hand, laser power and the particles do not get enough time to interact with each other at the low laser power and high scanning speed and thus produce a smaller molten pool. A smaller molten pool allows the zone to be solidified at a faster rate. The property of the repaired zone can be controlled by controlling the molten pool size which depends on the processing parameters.

4.2 Macrostructure Analysis

Figure 13(a) represents the standard repaired specimens for the Charpy impact test whereas **Figure 13(b)** shows the optical image of the repaired zone at low magnifications. From these figures, it is evident that whenever a new layer is deposited on the previous layer or the substrate, it melts a certain portion of the previous layer or substrate. The side or corner portion of the molten pool is considered as the defect prone area because of its comparatively lower capability of absorbing laser power. As a result, some of the powder particles do not melt completely. No defects on the surface of the repaired specimens have been observed through visual inspection. Moreover, the low magnification optical image provides the repaired area with a negligible defect. Only the proper selection and optimization of the processing parameters can ensure a defect-free repaired surface or the repaired surface with minimum defects. In this work, the processing parameters for repairing have been optimized successfully and thus have resulted in defects-free repaired specimens.

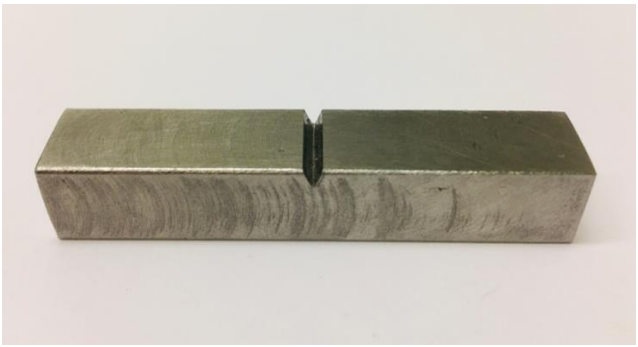

(a)

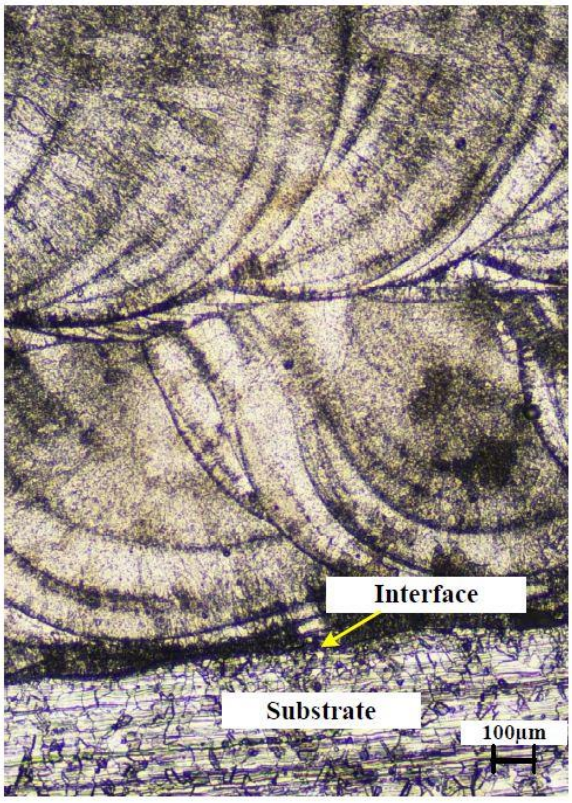

(b)

Figure 13: (a) Standard repaired specimen for Charpy impact test (b) optical images of the repaired zone.

4.3 Microstructure Evolution

Figure 14 shows the SEM micrograph, indicating the repaired zone, bonding zone, and substrate. The bright white stripe in the bonding zone is defined as the interface layer that is generated due to the interdiffusion between the substrate and the repaired zone. The optical images of the

repaired specimen is illustrated in **Figure 15**. **Figure 15 (a)** represents strong bonding between the repaired zone and the substrate, whereas **Figure 15 (b-c)** shows the grain structure inside the repaired zone. The columnar grain starts to initiate from the molten pool boundary and moves towards the center. The center portion is mainly consisting of equiaxed grain structure and moves towards the top. The different grain structures are a result of the difference in temperature gradient that varies from portion to portion inside the molten pool.

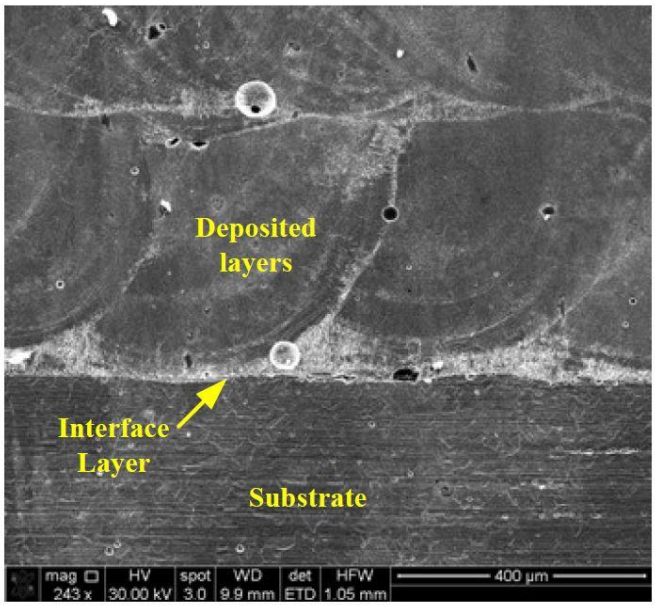

Figure 14: SEM micrograph representing the bonding zone, substrate, and repaired area of the repaired specimen.

Figure 16 shows the SEM micrographs of the microstructure of the repaired zone. From **Figure 16 (c-f),** it is obvious that the molten pool inside the repaired area consists of columnar and equiaxed grain structure. The growth of the columnar and equiaxed grain varies according to the varying temperature gradient and solidification rate inside the repaired area of the repaired specimen. The columnar grains start to nucleate from the molten pool boundary and move toward the center. Near the center of the molten pool, the conversion from columnar to equiaxed grain structure has been started due to the decreasing temperature gradient and before reaching the top,

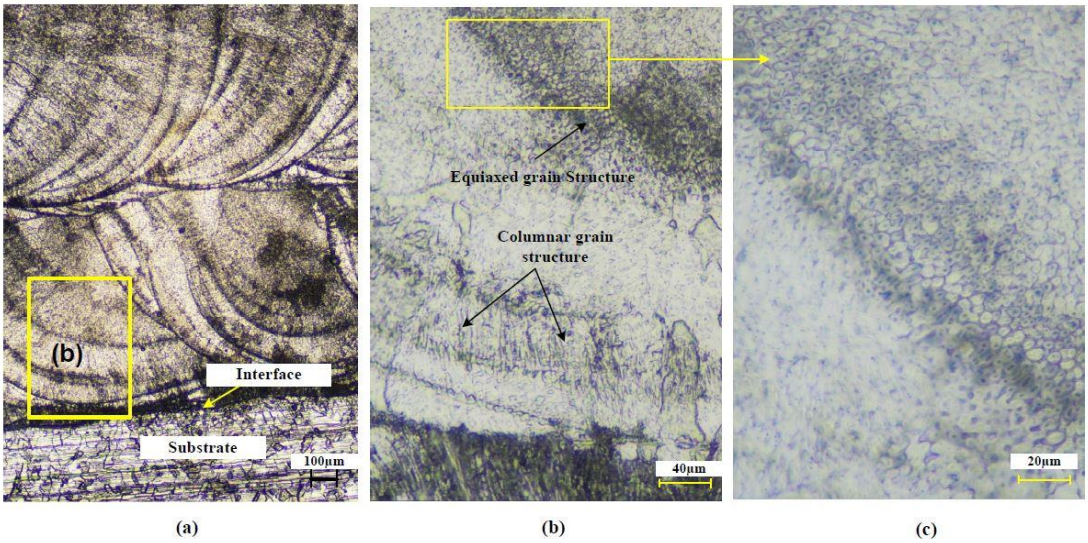

Figure 15: Optical images of the repaired zone; (a) bonding zone or interface in between the repaired zone and the substrate; (b-c) grain structure inside the molten pool of the repaired specimen.

all the columnar grains are converted into the equiaxed grain structure. The development of the microstructure, as well as the phase transformation, is initiated inside the repaired zone mainly due to the thermal gradient [54]. **Figure 16 (a)** represents the Heat Affected Zone (HAZ), which is found adjacent to the interface between the repaired zone and substrate. The length of the HAZ depends on the laser power and the scanning speed. With the increasing laser power and decreasing scanning speed, the length of the HAZ increases. The possible reason behind this is the size of the molten pool. If the molten pool is larger, it takes a long time to solidify and thus causes the HAZ to be greater in length. On the other hand, the lower laser power and higher scanning speed make the molten pool smaller in size. For the smaller molten pool, the solidification rate is comparatively higher, so the heat does not get enough time to propagate through the substrate. Therefore, the HAZ is smaller in length [55].

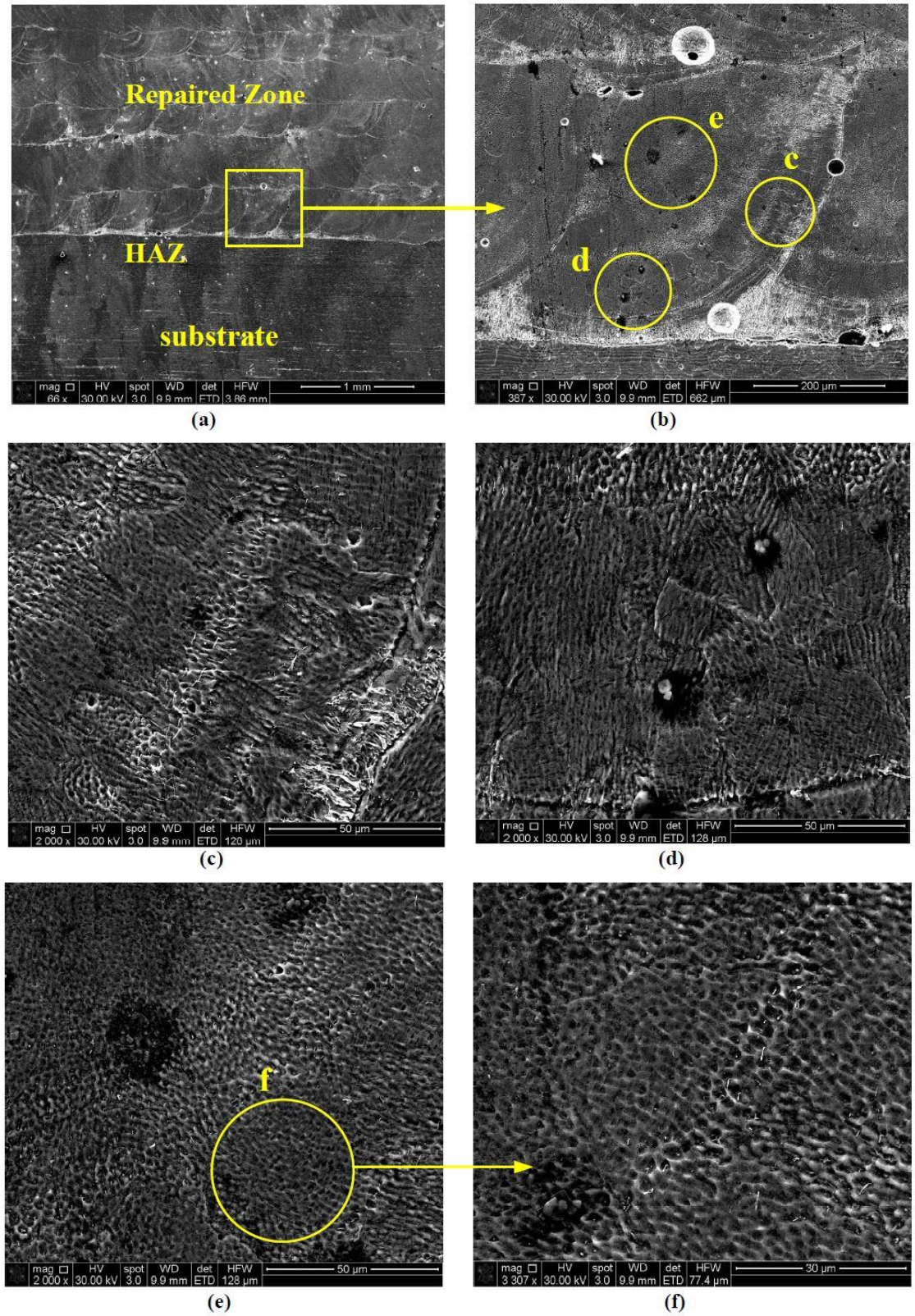

Figure 16: SEM micrographs of (a-b) repaired zone; (c-d) microstructure near the molten pool boundary, (e-f) microstructure at the center of the molten pool.

Figure 17 represents obvious pores inside the repaired area. During the repair process, it is a difficult task for the laser power to melt all the deposited powder particles properly near the molten pool boundary. This is why, in most cases, pores are found near the boundary of the molten pool. Sometimes shielding gas, which is used to prevent the oxidation, is also entrapped inside the molten pool during the deposition and unable to escape before the solidification [56]. The powder particles are splattered on the liquefied particles inside the molten pool during deposition and form a melt ball after the rapid solidification. The melt ball acts as the possible source of the pore formation. Generally, it is observed that the melting rate of the deposited powder particles are low at the start and the end of the track. Therefore, the number of pores are found higher at the start and the end of the tracks.

Figure 18 shows the SEM micrographs of microcracks inside the repaired area. From the figure, it is evident that microcracks are profoundly spread throughout the track length. There are several possible reasons for the microcracks initiations inside the repaired area. Surfaces of the repaired area are experiencing residual stress due to the high solidification rate. The compression stress inhibits the macro-cracking in the repaired zone, whereas the tensile stress is responsible for the microcracking in the direction of the deposited track [45, 57]. Partially melted powder particles and melt balls are observed on the surface of the deposited layers, which is also considered as another possible source of the microcrack initiation. Moreover, high input energy can cause the initiation of the microcrack inside the repaired zone [56]. According to the figure, the microcracks are more obvious in between the repaired area and substrate which makes it clear that the bonding between the deposited layers is comparatively stronger. The difference of the metallurgical composition between the substrate and the repaired area initiates the microcracks in between the interface of the repaired area and the substrate than the interfaces in between the repaired area.

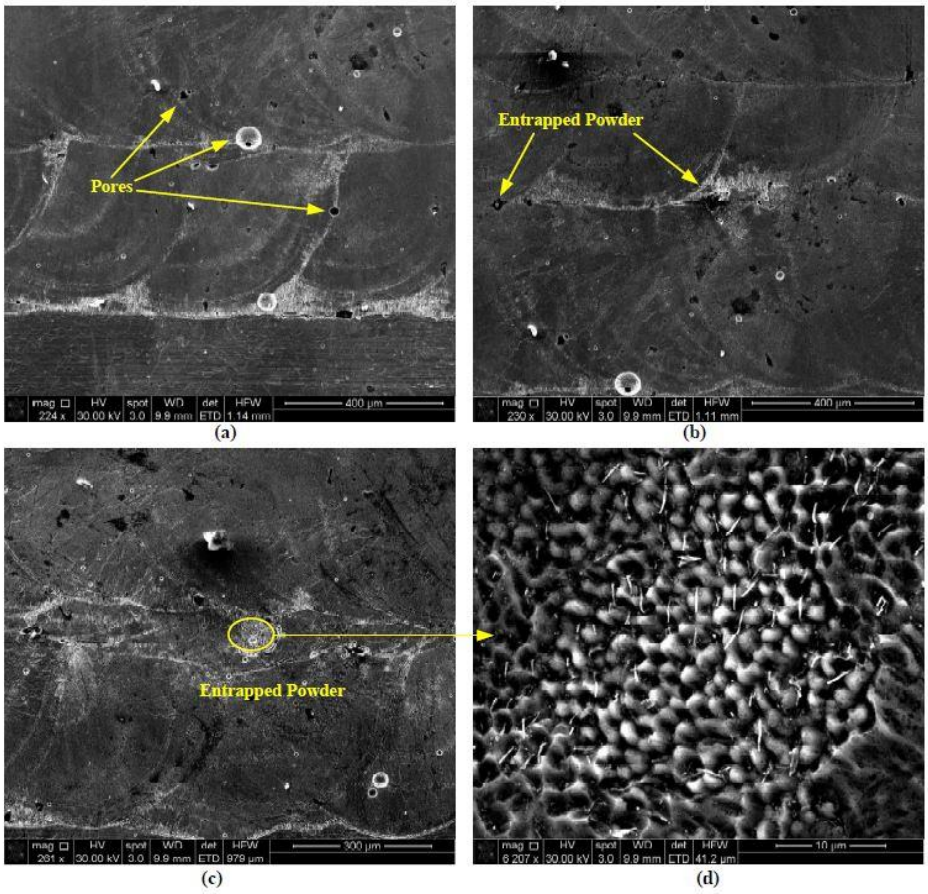

Figure 17: SEM micrographs of repaired zone; (a-b) possible pores (c-d) entrapped metal powder inside the repaired area.

Figure 19 provides the evidence of the metallurgical compositional difference in between the repaired area and the substrate through the Energy-Dispersive X-Ray Spectroscopy (EDS) analysis. Actually, when the deposited hot and melted powder particles come into contact with the substrate, they melt a certain portion of the substrate. Therefore, elements from both deposited metal powder and substrate are diluted into each other and deviate from their original chemical composition. As an outcome, continuous microcracks are found in the interface of the repaired area and the substrate. To further investigate, a line scan and an area scan, are performed in the interface. Both the line scan and area mapping provide identical results. From the EDS analysis, the non-uniform distribution of the nickel and manganese is apparent in the interface. Moreover,

there is a small segregation of silicon and sulphur in the interface. Apart from these elements, the rest of the alloying elements are distributed uniformly in the interface (**Figure 19**). Uniform distribution of the alloying elements with a little segregation can be obtained with a higher cooling rate [26].

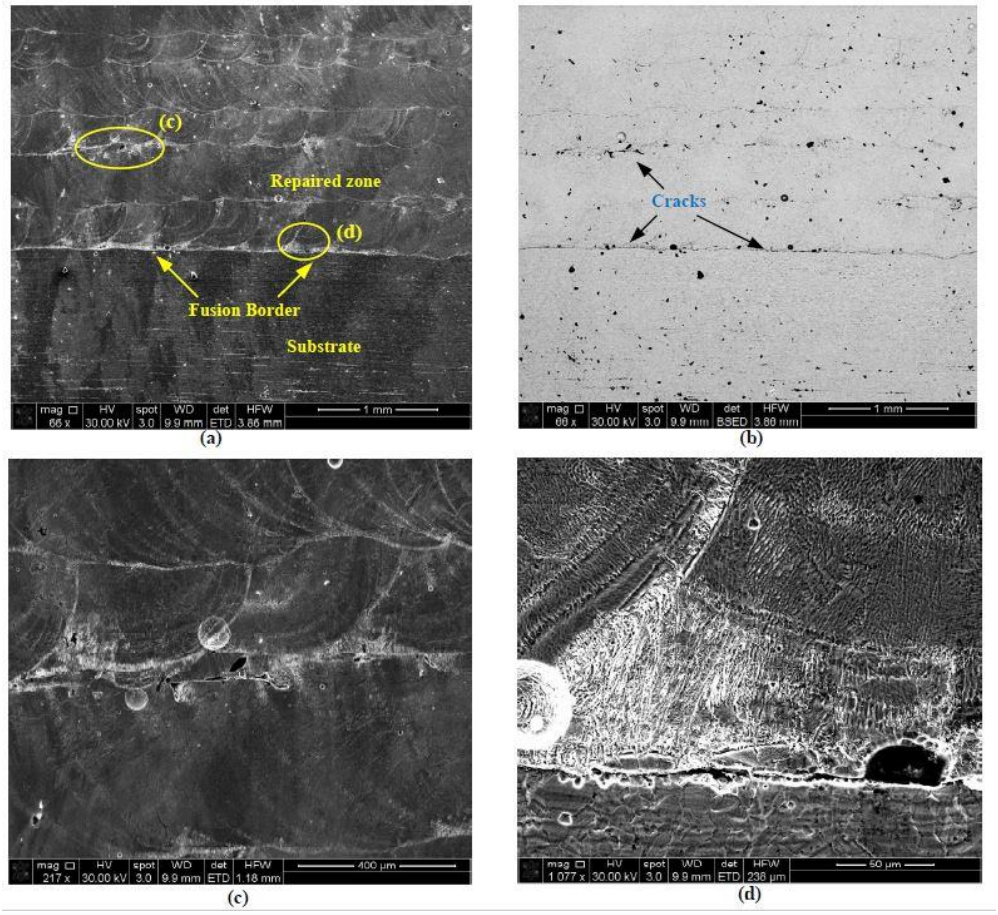

Figure 18: SEM micrographs of the microcracks inside the repaired area of the repaired specimen.

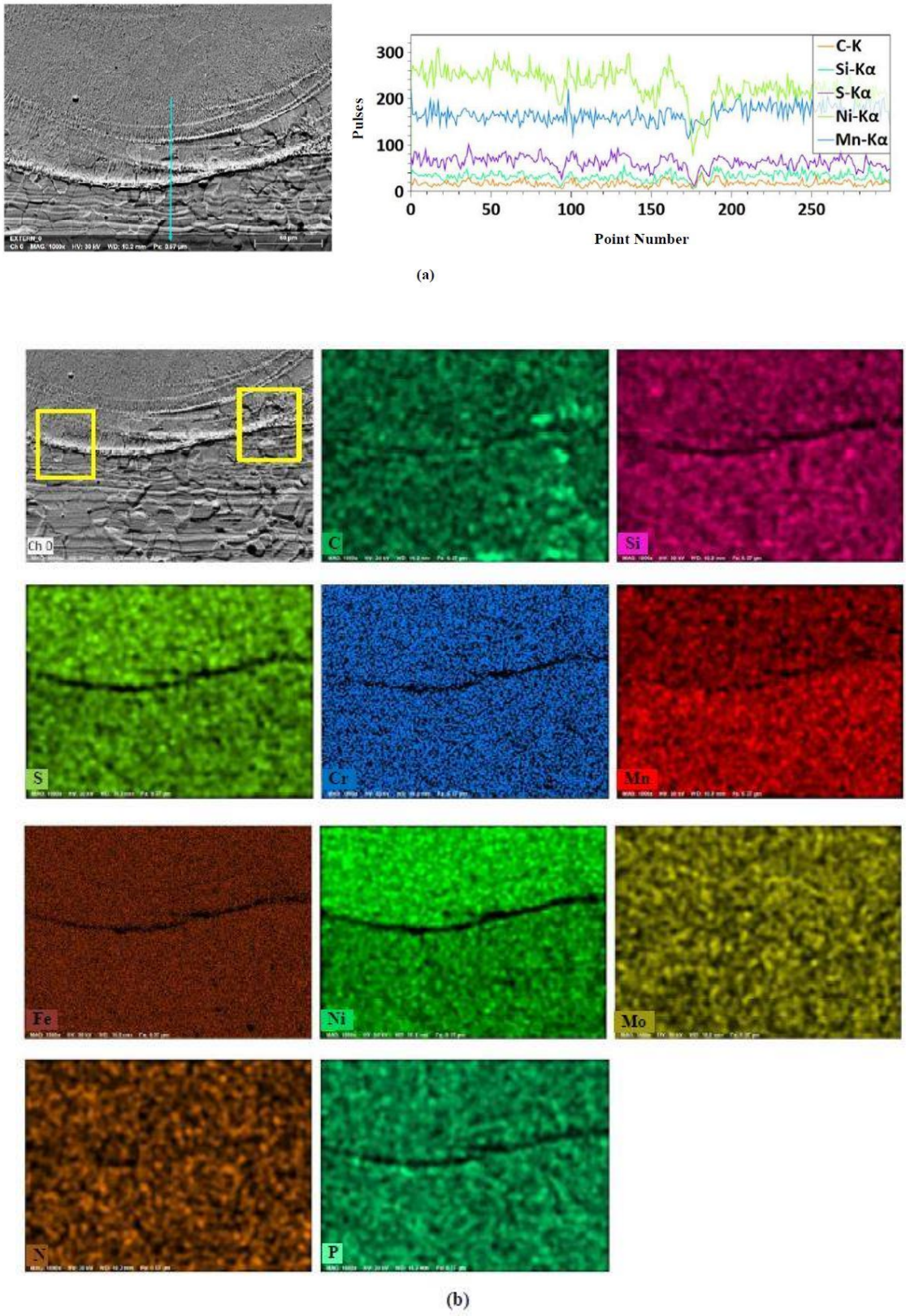

Figure 19: EDS analysis of repaired specimen interface (a) line scan (b) area scan map.

It is always recommended to deposit the same powder material on the substrate during the repair process to obtain better bonding. In this work, although the same metal powder and substrate (AISI 316L stainless steel) are used, the bonding in between the repaired zone and substrate is not strong enough. This is because the metallurgical compositional differences between the deposited area and substrate leave continuous microcracks in the interface of the repaired specimen. So whenever any cracks come into contact with these continuous microcracks, it is very easy for the cracks to be spread out in the directions same as interface across the specimen.

4.4 Microhardness Analysis

The profile of the microhardness of the repaired specimen is shown in **Figure 21,** where the analysis is done along the direction from the top of the deposited layers towards the end of the substrate. The microhardness measurement is performed along the centerline of the cross-section of the repaired specimen as shown in **Figure 20**. The starting point from where the measurement of the microhardness has been started is considered as the zero reference point and a constant distance of 0.635 mm is maintained throughout the measurement with a constant load of 300 gf. The repaired specimen is divided into three different zones, which are the repaired zone, the HAZ and the substrate as shown in **Figure 21**. The highest microhardness is obtained in the HAZ (about 218HV), followed by the repaired zone and substrate [42, 58]. The range of microhardness in the repaired zone is about 192-209HV, whereas the range of microhardness in the substrate is about 168-198HV. Although the same processing parameters are used during the repair process, the microhardness throughout the repaired zone is not homogeneous.

The optimized processing parameters have a great impact on the microhardness of the repaired zone. Thermal stress is developed inside the repaired zone due to the continuous heating

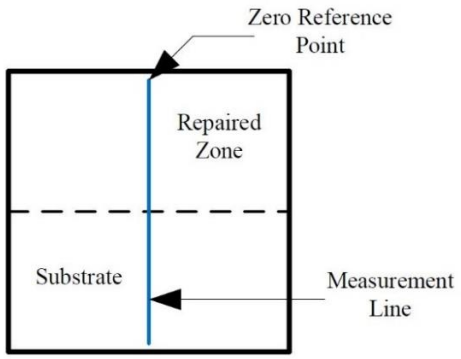

Figure 20: Schematic diagram of the microhardness measurement line on the cross-section of the repaired specimen.

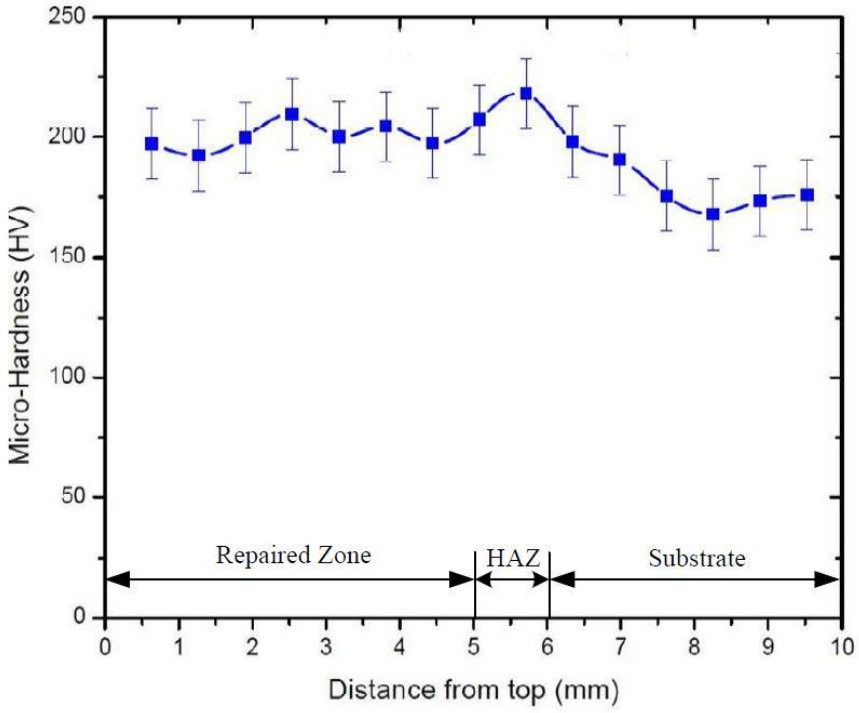

Figure 21: Microhardness profile along the depth direction of the repaired specimen.

and cooling during the deposition process, and therefore, the dislocation density is increased. Generally, the repaired zone exhibits the decreasing microhardness, whereas the HAZ shows better microhardness with increasing laser power. Similarly, higher scanning speed results in a higher microhardness of the repaired zone. Moreover, the microhardness decreases with the

increasing distance from the first deposited layer towards the top deposited layers. At the very initial stage of the deposition process, the quenching effect is found to be very high because of the rapid conduction of the heat through the substrate, and it decreases as the energy source moves away from the substrate [59].

4.5 Instrumented Charpy Impact Behavior

Impact property is considered one of the key properties for investing the quality of the repaired specimen. The selection and optimization of the processing parameters play an important role in getting a better impact property of the repaired specimen.

4.5.1 Charpy Impact Toughness

The Charpy impact toughness test is carried out at room temperature for all the specimens. **Figure 22** represents the fracture surface of all the specimens immediately after the Charpy impact test. The as-received specimens show the smooth fracture surface morphology where the crack starts from the tip of the notch and propagates down in a proper manner [**Figure 22(a**)]. This type of fracture resembles the characteristics of the ductile fracture. However, the repaired specimen shows the brittle fracture morphology. For repaired specimens, the crack starts from the tip of the notch, and on its way down towards the substrate, it comes in contact with many defects and tries to propagate in these directions. Since defects are not strong enough to support the crack propagation, so the crack could not spread out that much across the repaired specimen. Finally, when the crack comes in contact with the interface between the deposited area and substrate, it starts to propagate through the interface across the specimen, and the final fracture happens as shown in **Figure 22(b). Figure 22(c-d)** represents the fracture surface of a fully AM fabricated subsize specimen and the repaired subsize specimen respectively. The fracture surface of both AM (subsize) and RS (subsize) is not smooth, i.e. both exhibiting the brittle fracture characteristics. RS (subsize) behaves in a similar manner as the other repaired specimens.

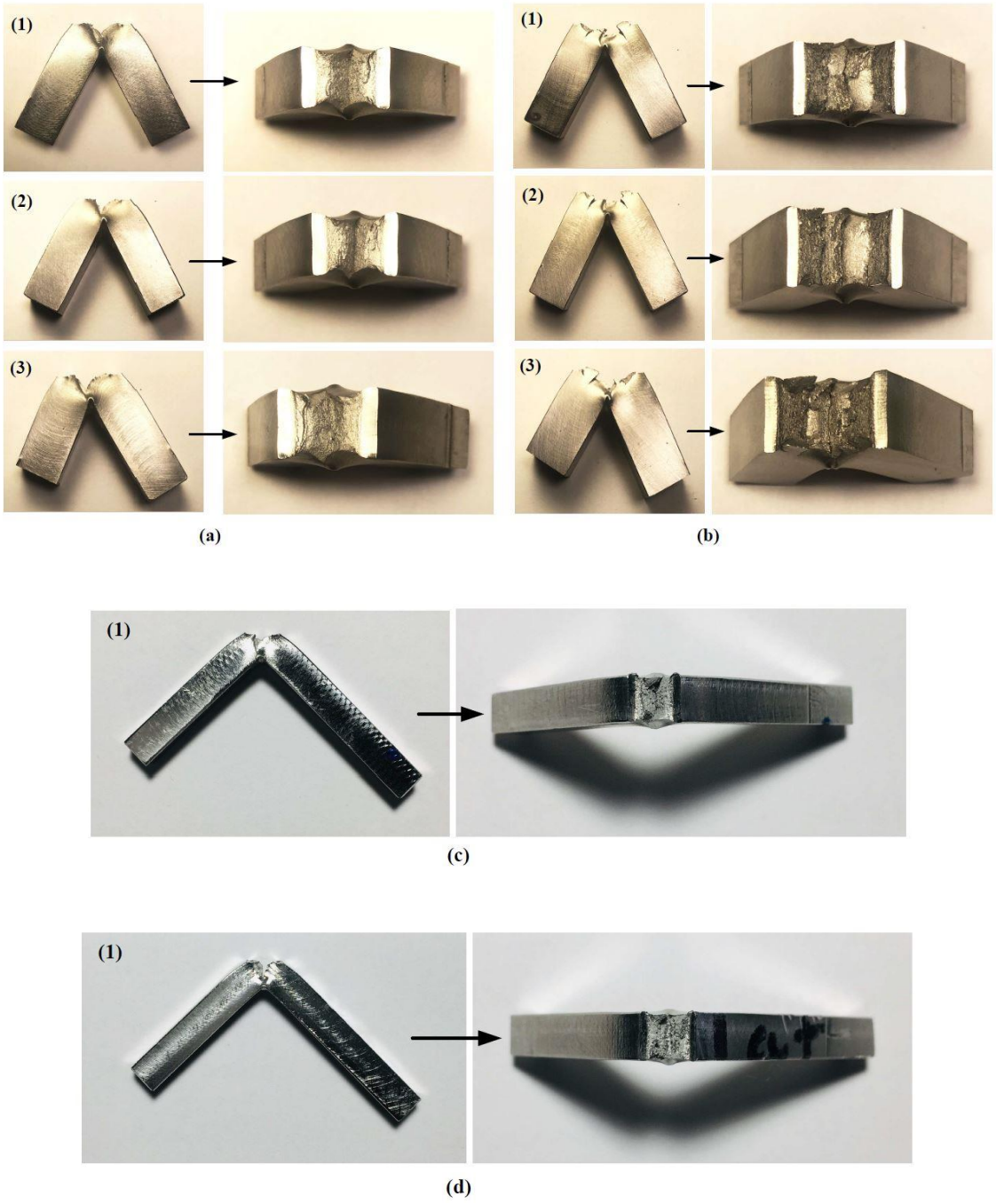

Figure 22: Fracture surface images of (a) as-received specimen (b) repaired specimen (c) AM (subsize) specimen (d) repaired (subsize) specimen. [AR= As-Received; RS= Repaired Specimen; AM=Additive Manufactured].

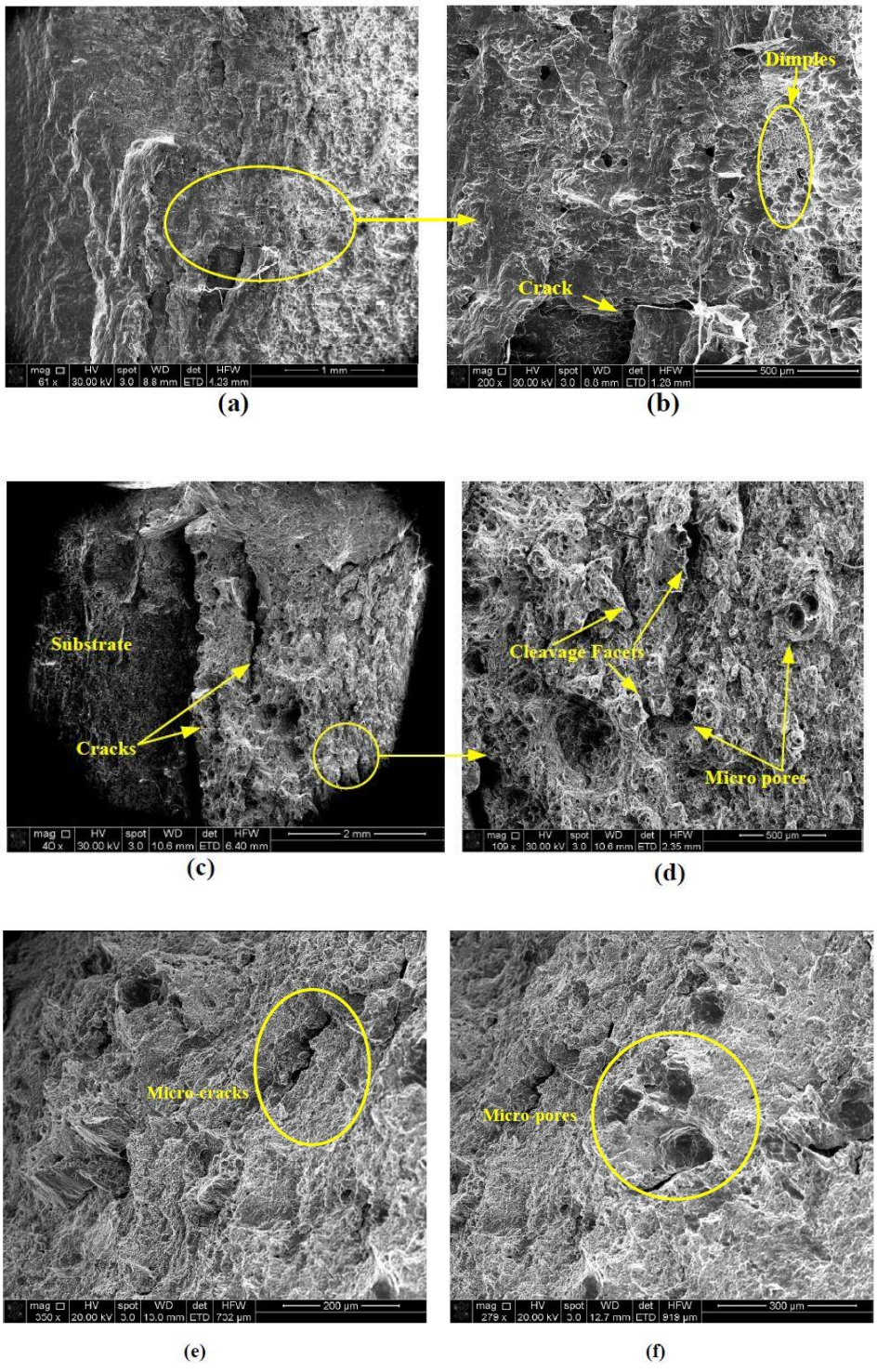

Figure 23: SEM micrographs of the fracture surface of the (a-b) as-received specimen (c-d) repaired specimen (e-f) AM (subsize) specimen. [AR= As-Received; RS= Repaired Specimen; AM=Additive Manufactured].

Figure 23 represents the SEM micrographs of the fracture surface of as-received, repaired and AM (subsize) specimens. **Figure 23 (a-b)** represents the SEM micrographs of the fracture surface of as-received specimens. Dimples on the fracture surface of the as-received specimen generally inhibit the propagation of microcracks and thus result in good impact property [60]. Although one or two microcracks are found on the fracture surface, their effects are not influential. From **Figure 23 (c-d)** it is obvious that the presence of microcracks, microvoids and cleavage facets on the fracture surface allows the repaired specimen to fail in a brittle manner. Moreover, the fracture surface of the AM (subsize) specimen is not free from defects which is clear from **Figure 23 (e-f).**

4.5.2 *Load-Deflection Curve Analysis*

The load-deflection curve is obtained as a result of the instrumented Charpy impact test which provides information about the amount of energy absorbed by each specimen. The impact specimen is placed on the anvil and hit by the hammer with a velocity of 5.25 m/s on the backside of the specimen as shown in **Figure 24.** When the hammer hits the specimen, the specimen starts to consume the energy and deform accordingly. The difference between the original shape and the shape immediately after the fracture or ejection is taken into consideration to determine the deformation volume. The longitudinal section looks like an envelope shape around the tip of the hammer soon after the deformation. **Figure 25** shows how the deformation of the specimen occurs with the applied load.

Figure 26 shows a standard schematic load-deflection curve and the corresponding energy at each phase of the load [61]. According to the figure, F_{gy} is the general yield load, F_m is the maximum load, F_{bf} is the initiation load of unstable crack propagation, and F_a is the load at the end of the unstable crack propagation (arrest force). When the hammer hits the specimens, it

starts to deform elastically and continues proportionally up to a point F_{gy}. As it crosses the point F_{gy}, it starts to deform plastically until it reaches the point F_m. This point indicates the maximum

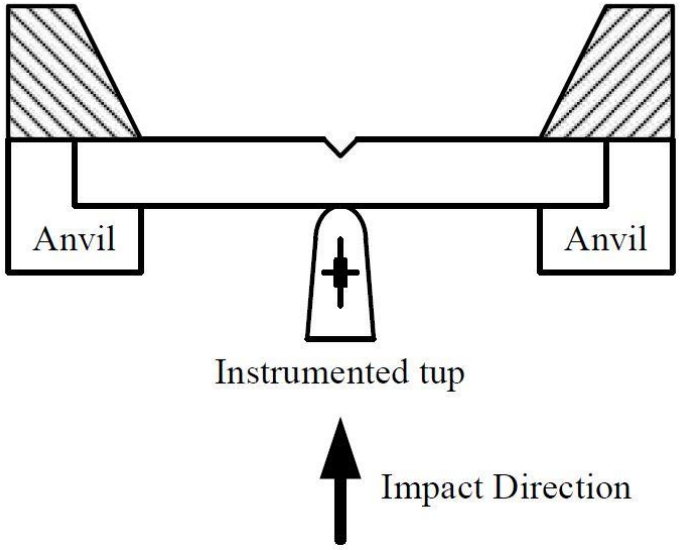

Figure 24: Schematic set up for instrumented Charpy Impact test.

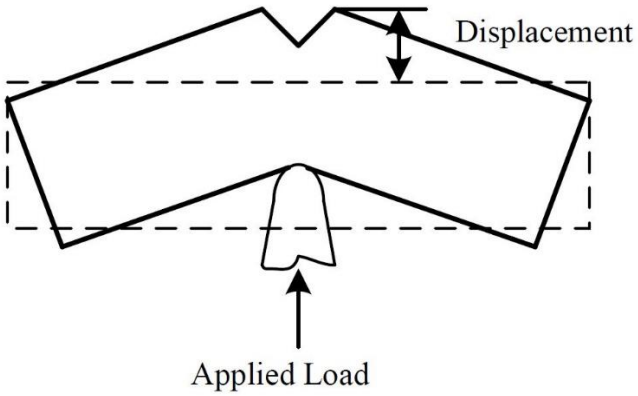

Figure 25: The schematic diagram for measuring the load-displacement at the notch mouth [62].

load that can be absorbed by the specimen without any initiation of cracks. F_m is the point, after which small cracks are started to initiate inside the specimen. As the cracks grow in length with time, the volume of deformation decreases, respectively. The area in between F_m and F_{bf} is the area where the cracks grow in a stable manner. From the figure, it is evident that after the F_{bf}

point, there is a sharp decrease in the load, and the potential reason behind that is the unstable crack propagation. The rate of unstable crack propagation is faster than the stable crack propagation. Finally, F_a is known as the arrest point, after which the specimen fails permanently.

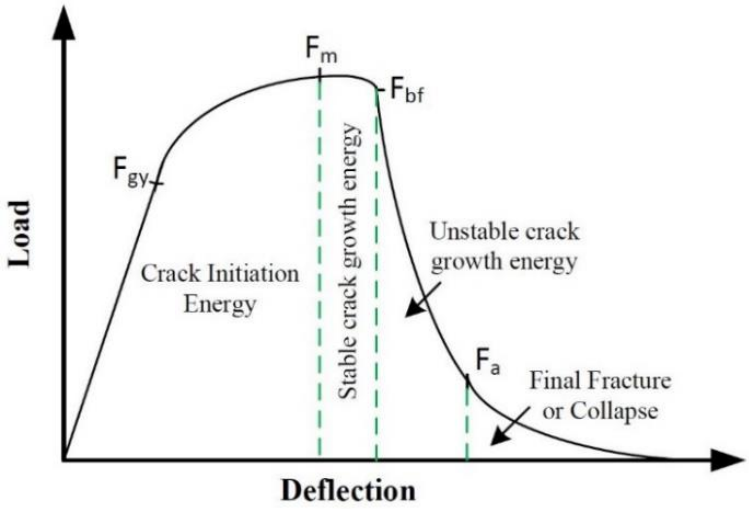

Figure 26: A standard schematic diagram symbolizing the different phases of the load as a function of deflection [61].

Figure 27 exhibits the graphical representation of the energy absorbed by the specimens [RS, AR, AM (subsize) and RS (subsize)]. From the figure, it is evident that all the specimens show almost the same characteristics up to the maximum load absorption point. The repaired specimen (RS1, RS2, and RS3) show higher peaks (F_m) in comparison to others, as depicted in the figure. F_m is the point after which the cracks start to initiate and propagate in a stable and unstable manner respectively. The area of stable crack propagation is very negligible for the repaired specimen (RS1, RS2, and RS3), whereas the as-received specimens (AR1, AR2, and AR3) exhibit good stable crack propagation area. Therefore, the total energy absorbed by the as-received specimens (AR1, AR2, and AR3) is higher. In the case of the repaired specimen (RS1, RS2, and RS3), as soon the cracks reach the interface (in between the substrate and repaired zone), specimens fail immediately after because the interface is highly the crack-prone. Other

interfaces inside the deposited zone also have some defects, they are not strong enough to support the cracks towards the final fracture. On the other hand, the absence of defect-prone areas inside the as-received specimens makes it convenient for the cracks to propagate in a proper manner and thus results in higher energy absorption. The interface (in between the substrate and deposited

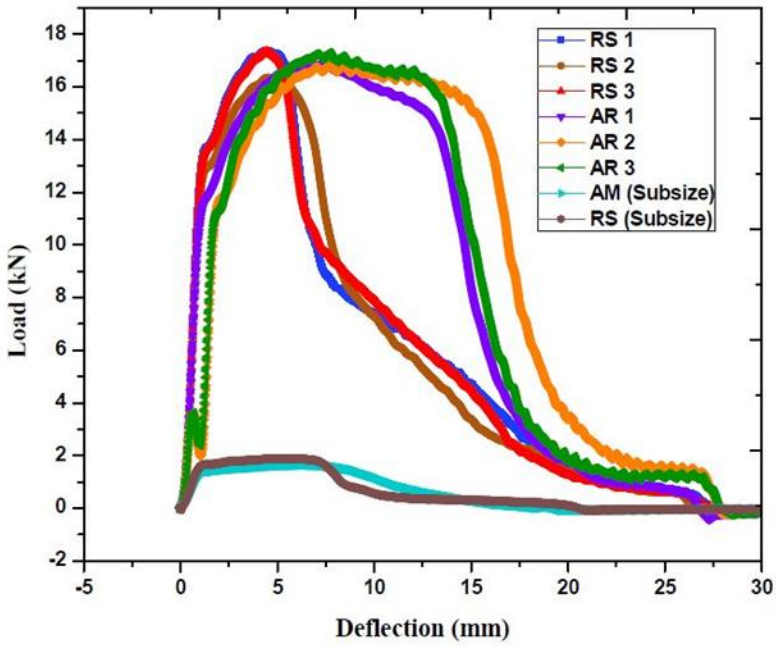

Figure 27: Load vs. deflection curve for as-received, repaired specimen, AM (subsize) specimen, and repaired (subsize) specimen. [AR= As-Received; RS= Repaired Specimen; AM= Additive Manufactured].

area) is mainly responsible for the lower energy absorption characteristic which is also experienced by RS (subsize) specimen. Although there are so many defects inside AM (subsize) specimen, it still shows better results than the RS (subsize). The potential reason is the absence of a defect prone interface unlike the RS (subsize). Moreover, the geometry of the repaired specimen has a great impact on the amount of energy absorbed. In standard repaired specimens (RS1, RS2, and RS3), a 5mm deposition is performed on the top of the 5mm substrate whereas, for the RS (subsize), a 3mm deposition is performed on the top of the 2mm substrate. So, in RS (subsize) the

cracks get more time to propagate before the final fracture has taken place through the interface (in between the substrate and deposited area) across the specimen. Thus, the higher the thickness of the depositing area in comparison to substrate thickness, the higher the possibility of getting a good impact property. The amount of energy absorbed by each specimen has a direct correlation with the time it requires to fail permanently. **Table 6** illustrates the time required to reach the maximum load and permanent fracture. As per the table, the time required for the permanent fracture of the as-received specimens is longer than the repaired specimens.

Table 6: The required time for the maximum load (F_m) and complete fracture.

Specimens	**Maximum load (N), F_m**	**Time to reach maximum load (ms)**	**Total fracture time (ms)**
AR 1	16886	1.38	6.57
AR 2	16845	1.53	7.02
AR 3	17295	1.53	6.89
RS 1	17373	0.86	6.26
RS 2	16352	0.88	5.97
RS 3	17340	0.86	6.17
AM (Subsize)	1652	1.15	3.71
RS (Subsize)	1900	1.00	3.97

Figure 28 (a) through **(h)** represents the load-deflection curves of the as-received specimens (AR1, AR2, and AR3), repaired specimens (RS1, RS2, and RS3), AM (subsize) and repaired specimen (subsize) separately. The total energy absorbed by the specimen can be divided into two parts: initiation energy (E_I) and propagation energy (E_P) [35]. Before F_m, the area under the curve represents the initiation energy (E_I), and the area after F_m is called the propagation energy (E_P). The initiation energy is determined by measuring the area under the curves up to F_m, whereas the propagation energy is determined by measuring the area under the curve from F_m to the end [63-65]. Figure 28 (g) and (h) represents the curve for AM (subsize) and RS (subsize), respectively, and their respective amount of energy absorption. Although both of them are showing the brittle

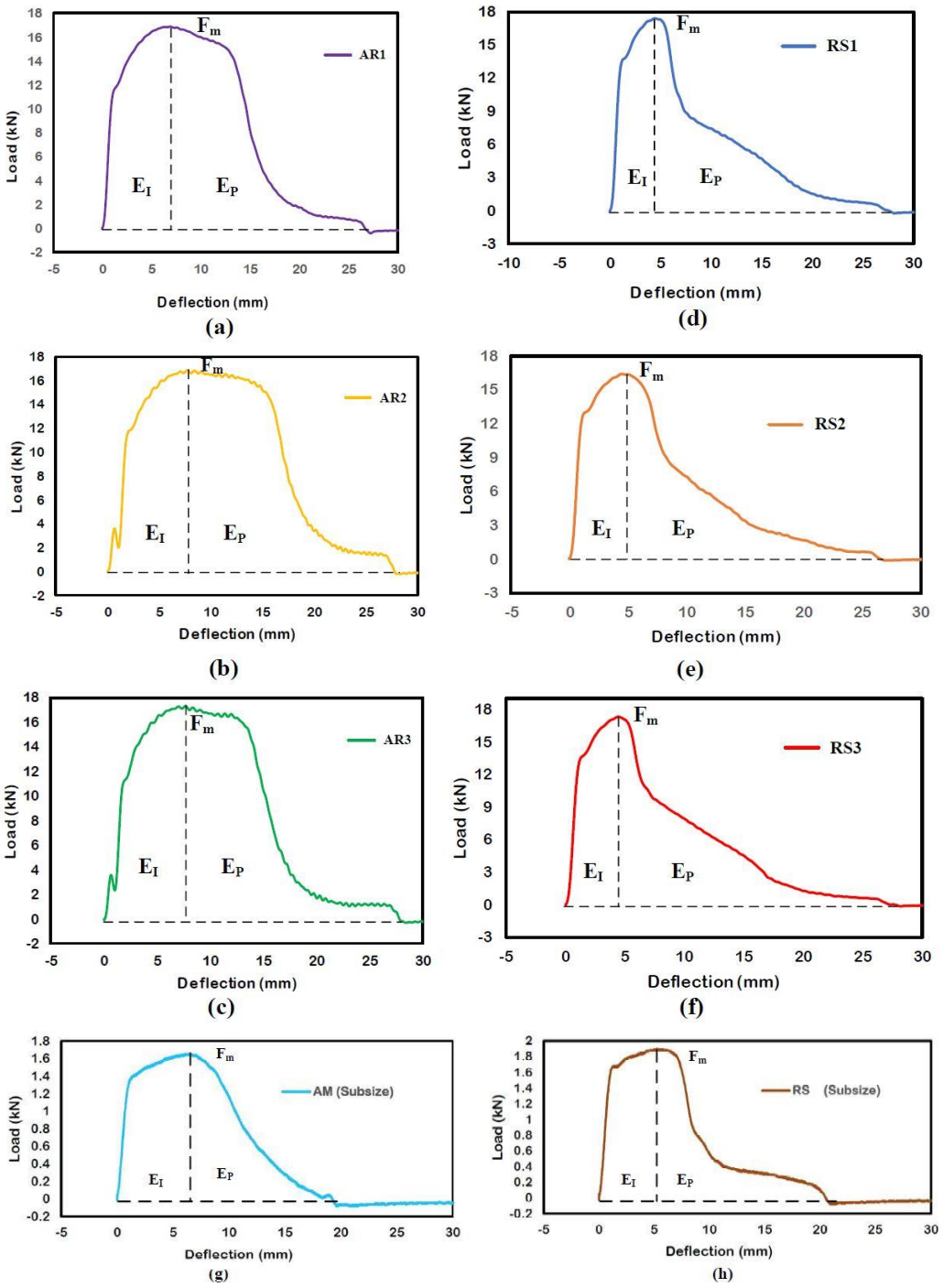

Figure 28: Impact energy analysis from the load-deflection curves obtained from instrumented charpy impact test of the (a-c) as-received specimen (d-f) repaired specimens (g) AM (subsize) specimen (h) repaired (subsize) specimens. [AR= As-Received; RS= Repaired Specimen; AM= Additive Manufactured].

fracture behaviors, the amount of energy absorbed by AM (subsize) specimen is higher. The potential reason is the absence of interface in AM (subsize) specimen.

Figure 29 provides the bar chart of the total energy absorbed by the different specimens. From the figure, it is clear that the energy absorbed by the as-received specimen is higher than the repaired specimens. Moreover, the propagation energy is dominant over initiation energy for every specimen. Although the laser processing parameters are kept constant during the repair process, the energy absorbed by the different repaired specimens vary. The number of possible defects (i.e., pores, cracks, etc.) inside the deposited zone makes the difference in between them. Sometimes high angle boundaries of the martensite crystal help to prohibit the microcrack propagation, and this might be a possible reason for the variation in the total absorbed energy [66]. Specific energy distribution for each load-deflection curve of different specimens is listed in **Table 7.**

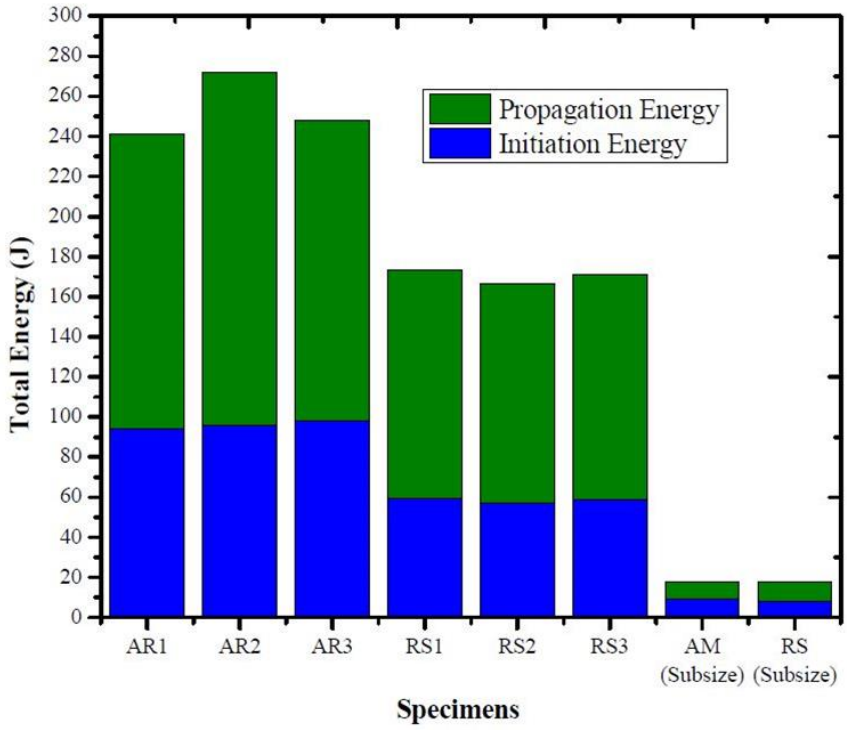

Figure 29: Initiation and propagation energy of different specimens obtained from the load-deflection curve of the instrumented Charpy impact test. [AR= As-Received; RS= Repaired Specimen; AM= Additive Manufactured].

Table 7: The initiation and propagation energy of different specimens.

Specimens	**Initiation Energy (E_I), J**	**Propagation Energy (E_P), J**	**Total Energy, J**
RS1	60	114	173
RS2	57	110	167
RS3	59	112	171
AR1	94	147	241
AR2	96	176	272
AR3	98	150	248
AM (Subsize)	9	9	18
RS (Subsize)	8	9	17

CHAPTER 5

CONCLUSIONS

In this work, stainless steel 316L has been repaired by depositing the stainless steel 316L powder utilizing the DED process. The microstructure, impact property and fracture morphology of the repaired specimen have been investigated. The major outcomes of this study are summed up as follows:

(a) The specimens are repaired successfully by utilizing the DED process with the proper selection and the optimization of processing parameters. No defects have been found in the repaired specimen through visual inspection. However, optical images and SEM micrographs represent some obvious pores and microcracks inside the repaired zone. Generally, pores are formed near the molten pool boundary because of the presence of the partially melted powder particle after the rapid solidification. Moreover, trapped shielding gas in the molten pool and the melt ball are the potential reason of pores formation. Residual stress and difference in the metallurgical composition are the potential reason of the microcrack initiation through the interfaces in the repaired zone.

(b) The microstructure of the repaired zone mainly contains columnar and equiaxed grain structures. The columnar grain structure is formed near the molten pool boundary, whereas the equiaxed grain structure is formed in the center region depending on the variation of the temperature gradient.

(c) The microhardness of the HAZ is about 218HV which is higher than both repaired zone and substrate. The microhardness of the repaired zone and substrate is within the ranges of 192-209HV and 168-198HV, respectively.

(d) The Charpy impact test is performed at room temperature, and the results show that the as-received specimens represent better impact property than the repaired specimens. The average impact energy of the repaired specimens is roughly observed 70% of the as-received specimen. The defects inside the repaired zone and interface effects result in lower energy absorption by the repaired specimens. The energy absorbs by the subsize specimen is lower than the as-received specimen as well. Moreover, the percentage of propagation energy is higher than the initiation energy for each specimen. From the fracture surface morphology, it is evident that the as-received specimens show the ductile fracture characteristics, whereas the repaired specimens represent the brittle fracture characteristics.

`

REFERENCES

[1] Balsone, S., M. Khobaib, and G. Watt, *The Effect of Stress on the Hot Corrosion of Inconel 718*. 1985: Metallurgical Soc. of AIME.

[2] Kaysser, W., *Surface modifications in aerospace applications.* Surface engineering, 2001. **17**(4): p. 305-312.

[3] Kathuria, Y., *Some aspects of laser surface cladding in the turbine industry.* Surface and Coatings Technology, 2000. **132**(2-3): p. 262-269.

[4] Lin, X., et al., *Microstructure and mechanical properties of laser forming repaired 17-4PH stainless steel.* Materials Science and Engineering: A, 2012. **553**: p. 80-88.

[5] King, A.M., et al., *Reducing waste: repair, recondition, remanufacture or recycle?* Sustainable development, 2006. **14**(4): p. 257-267.

[6] Leino, M., J. Pekkarinen, and R. Soukka, *The role of laser additive manufacturing methods of metals in repair, refurbishment and remanufacturing–enabling circular economy.* Physics Procedia, 2016. **83**: p. 752-760.

[7] Commission, E., *Closing the loop–An EU action plan for the circular economy.* 2015 COM (2015) 614 final, 2015.

[8] Pattnaik, R., *Investigation into compatibility between repair material and substrate concrete using experimental and finite element method.* 2006.

[9] *Steels Grades and Properties*. [cited 2019 August 21]; Available from: https://www.thebalance.com/steel-grades-2340174.

[10] de Lima, M.S.F. and S. Sankaré, *Microstructure and mechanical behavior of laser additive manufactured AISI 316 stainless steel stringers.* Materials & Design, 2014. **55**: p. 526-532.

[11] Schaeffler, A.L., *Constitution diagram for stainless steel weld metal.* Metal progress, 1949. **56**(11): p. 680.

[12] Guo, P., et al., *Study on microstructure, mechanical properties and machinability of efficiently additive manufactured AISI 316L stainless steel by high-power direct laser deposition.* Journal of Materials Processing Technology, 2017. **240**: p. 12-22.

[13] *Type 316 and 316L Stainless Steels*. [cited 2019 August 21]; Available from: https://www.thebalance.com/type-316-and-316l-stainless-steel-2340262.

[14] Champagne, V.K., *The cold spray materials deposition process: fundamentals and applications*. 2007: Elsevier.

[15] Gunaraj, V. and N. Murugan, *Application of response surface methodology for predicting weld bead quality in submerged arc welding of pipes.* Journal of Materials Processing Technology, 1999. **88**(1-3): p. 266-275.

[16] Mahan, J.E., *Physical vapor deposition of thin films.* Physical Vapor Deposition of Thin Films, by John E. Mahan, pp. 336. ISBN 0-471-33001-9. Wiley-VCH, January 2000., 2000: p. 336.

[17] Li, W., et al., *Solid-state additive manufacturing and repairing by cold spraying: A review.* Journal of materials science & technology, 2018. **34**(3): p. 440-457.

[18] Petráčková, K., J. Kondás, and M. Guagliano, *Fixing a hole (with cold spray).* International Journal of Fatigue, 2018. **110**: p. 144-152.

[19] Huang, C., et al., *Advanced brass-based composites via cold-spray additive-manufacturing and its potential in component repairing.* Surface and Coatings Technology, 2019.

[20] Widener, C.A., O.C. Ozdemir, and M. Carter, *Structural repair using cold spray technology for enhanced sustainability of high value assets.* Procedia Manufacturing, 2018. **21**: p. 361-368.

[21] Villafuerte, J., *Modern cold spray: materials, process, and applications*. 2015: Springer.

[22] Yin, S., et al., *Cold spray additive manufacturing and repair: Fundamentals and applications.* Additive Manufacturing, 2018. **21**: p. 628-650.

[23] Frazier, W.E., *Metal additive manufacturing: a review.* Journal of Materials Engineering and Performance, 2014. **23**(6): p. 1917-1928.

[24] Technologies, A.C.F.o.A.M. and A.C.F.o.A.M.T.S.F.o. Terminology, *Standard terminology for additive manufacturing technologies*. 2012: ASTM International.

[25] Gibson, I., D.W. Rosen, and B. Stucker, *Additive manufacturing technologies*. Vol. 17. 2014: Springer.

[26] Oh, W.J., et al., *Repairing additive-manufactured 316L stainless steel using direct energy deposition.* Optics & Laser Technology, 2019. **117**: p. 6-17.

[27] Chew, Y., et al., *Microstructure and enhanced strength of laser aided additive manufactured CoCrFeNiMn high entropy alloy.* Materials Science and Engineering: A, 2019. **744**: p. 137-144.

[28] Liu, X.-B. and R.-L. Yu, *Microstructure and high-temperature wear and oxidation resistance of laser clad γ/W2C/TiC composite coatings on γ-TiAl intermetallic alloy.* Journal of alloys and compounds, 2007. **439**(1-2): p. 279-286.

[29] Liu, X.-B., et al., *Development and characterization of laser clad high temperature self-lubricating wear resistant composite coatings on Ti–6Al–4V alloy*. Materials & Design, 2014. **55**: p. 404-409.

[30] Moghaddam, N.S., et al., *Recent Advances in Laser-Based Additive Manufacturing.* Laser-Based Additive Manufacturing of Metal Parts: Modeling, Optimization, and Control of Mechanical Properties, 2017.

[31] Mazumder, J., *Laser-aided direct metal deposition of metals and alloys*, in *Laser Additive Manufacturing*. 2017, Elsevier. p. 21-53.

[32] Shi, Q., et al., *Effects of laser processing parameters on thermal behavior and melting/solidification mechanism during selective laser melting of TiC/Inconel 718 composites.* Optics & Laser Technology, 2016. **84**: p. 9-22.

[33] Liu, Q., et al., *TC17 titanium alloy laser melting deposition repair process and properties.* Optics & Laser Technology, 2016. **82**: p. 1-9.

[34] Petrat, T., et al., *Laser metal deposition as repair technology for a gas turbine burner made of Inconel 718.* Physics Procedia, 2016. **83**: p. 761-768.

[35] Kumar, L.J. and C.K. Nair, *Laser metal deposition repair applications for Inconel 718 alloy.* Materials Today: Proceedings, 2017. **4**(10): p. 11068-11077.

[36] Kistler, N.A., et al., *Effect of processing conditions on the microstructure, porosity, and mechanical properties of Ti-6Al-4V repair fabricated by directed energy deposition.* Journal of Materials Processing Technology, 2019. **264**: p. 172-181.

[37] Graf, B., A. Gumenyuk, and M. Rethmeier, *Laser metal deposition as repair technology for stainless steel and titanium alloys.* Physics Procedia, 2012. **39**: p. 376-381.

[38] Paydas, H., et al., *Laser cladding as repair technology for Ti–6Al–4V alloy: Influence of building strategy on microstructure and hardness.* Materials & Design, 2015. **85**: p. 497-510.

[39] Pinkerton, A., W. Wang, and L. Li, *Component repair using laser direct metal deposition.* Proceedings of the Institution of Mechanical Engineers, Part B: Journal of Engineering Manufacture, 2008. **222**(7): p. 827-836.

[40] Song, L., et al., *Repair of 304 stainless steel by laser cladding with 316L stainless steel powders followed by laser surface alloying with WC powders.* Journal of Manufacturing Processes, 2016. **24**: p. 116-124.

[41] Zhang, X., et al., *Evaluation of component repair using direct metal deposition from scanned data.* The International Journal of Advanced Manufacturing Technology, 2018. **95**(9-12): p. 3335-3348.

[42] Marya, M., et al., *A Metallurgical Investigation of the Direct Energy Deposition Surface Repair of Ferrous Alloys.* Journal of Materials Engineering and Performance, 2018. **27**(2): p. 813-824.

[43] Sun, G., et al., *Microstructure and mechanical properties of HSLA-100 steel repaired by laser metal deposition.* Surface and Coatings Technology, 2018. **351**: p. 198-211.

[44] Sun, G., et al., *Laser metal deposition as repair technology for 316L stainless steel: Influence of feeding powder compositions on microstructure and mechanical properties.* Optics & Laser Technology, 2019. **109**: p. 71-83.

[45] Da Sun, S., et al., *Effect of laser clad repair on the fatigue behaviour of ultra-high strength AISI 4340 steel.* Materials Science and Engineering: A, 2014. **606**: p. 46-57.

[46] Sun, S.D., et al., *Evaluation of microstructure and fatigue properties in laser cladding repair of ultrahigh strength AerMet® 100 steel.* Journal of Laser Applications, 2015. **27**(S2): p. S29202.

[47] Lourenço, J.M., et al., *Fatigue and fracture behavior of laser clad repair of AerMet® 100 ultra-high strength steel.* International Journal of Fatigue, 2016. **85**: p. 18-30.

[48] Atwood, C., et al., *Laser spray fabrication for net-shape rapid product realization LDRD*. 1999, Sandia National Labs., Albuquerque, NM (US); Sandia National Labs ….

[49] Li, Y., et al., *The influences of processing parameters on forming characterizations during laser rapid forming.* Materials Science and Engineering: A, 2003. **360**(1-2): p. 18-25.

[50] Paul, C., et al., *Cobalt-free laser cladding on AISI type 316L stainless steel for improved cavitation and slurry erosion wear behavior.* Journal of materials engineering and performance, 2014. **23**(12): p. 4463-4471.

[51] Wang, W., et al. *Component repair using laser direct metal deposition*. in *Proceedings of the 35th International MATADOR Conference*. 2007. Springer.

[52] Ahmed, S.H. and A. Mian, *Influence of Material Property Variation on Computationally Calculated Melt Pool Temperature during Laser Melting Process.* Metals, 2019. **9**(4): p. 456.

[53] Cao, S., D. Gu, and Q. Shi, *Relation of microstructure, microhardness and underlying thermodynamics in molten pools of laser melting deposition processed TiC/Inconel 625 composites.* Journal of Alloys and Compounds, 2017. **692**: p. 758-769.

[54] Hunt, J., *Steady state columnar and equiaxed growth of dendrites and eutectic.* Materials science and engineering, 1984. **65**(1): p. 75-83.

[55] Mahamood, R.M. and E.T. Akinlabi, *Heat affected zone Relationship with processing parameter in Additive Manufacturing Process.* Materials Today: Proceedings, 2018. **5**(9): p. 18362-18367.

[56] Rashid, R.R., et al., *Metallurgical and geometrical characterisation of the 316L stainless steel clad deposited on a mild steel substrate.* Surface and Coatings Technology, 2017. **327**: p. 174-184.

[57] Moat, R., et al., *Residual stresses in laser direct metal deposited Waspaloy.* Materials Science and Engineering: A, 2011. **528**(6): p. 2288-2298.

[58] Zhang, K., et al., *Characterization of stainless steel parts by laser metal deposition shaping.* Materials & Design, 2014. **55**: p. 104-119.

[59] Yang, N., et al., *Process-structure-property relationships for 316L stainless steel fabricated by additive manufacturing and its implication for component engineering.* Journal of Thermal Spray Technology, 2017. **26**(4): p. 610-626.

[60] Vora, H.D., et al., *One-dimensional multipulse laser machining of structural alumina: evolution of surface topography.* The International Journal of Advanced Manufacturing Technology, 2013. **68**(1-4): p. 69-83.

[61] Ambriz, R., et al., *Fracture energy evaluation on 7075-T651 aluminum alloy welds determined by instrumented impact pendulum.* Transactions of Nonferrous Metals Society of China, 2016. **26**(4): p. 974-983.

[62] Tronskar, J., M. Mannan, and M. Lai, *Direct measurement of displacement in instrumented Charpy impact testing for structural integrity assessment.* Journal of testing and evaluation, 2001. **29**(3): p. 246-257.

[63] Chen, W.W. and B. Song, *Split Hopkinson (Kolsky) bar: design, testing and applications*. 2010: Springer Science & Business Media.

[64] Wullaert, R., *Impact Testing of Metals.* ASTM STP, 1970. **466**: p. 148-64.

[65] Liu, D., B. Cheng, and Y. Chen, *Strengthening and toughening of a heavy plate steel for shipbuilding with yield strength of approximately 690 MPa.* Metallurgical and Materials Transactions A, 2013. **44**(1): p. 440-455.

[66] Shome, M. and O. Mohanty, *Continuous cooling transformation diagrams applicable to the heat-affected zone of HSLA-80 and HSLA-100 steels.* Metallurgical and Materials Transactions A, 2006. **37**(7): p. 2159-2169.

VITA

SOUMYA MANDAL

Candidate for the Degree of

Master of Science

Thesis: IMPACT PROPERTIES OF AISI 316L STAINLESS STEEL REPAIRED BY DIRECTED ENERGY DEPOSITION (DED) ADDITIVE MANUFACTURING PROCESS

Major Field: Mechanical and Aerospace Engineering

Biographical:

Education:

Completed the requirements for the Master of Science in Mechanical and Aerospace Engineering at Oklahoma State University, Stillwater, Oklahoma in December, 2019.

Completed the requirements for the Bachelor of Science in Mechanical Engineering at Rajshahi University of Engineering & Technology, Rajshahi, Bangladesh in December, 2013.

Experience: Lecturer, Department of Mechanical Engineering, Rajshahi University of Engineering & Technology, Rajshahi, Bangladesh (January 2015 - December 2017).

Professional Memberships: Institution of Engineers (IEB), Bangladesh.